

ABSTRACT

Title of dissertation: THE EFFECT OF BORIC ACID ON THE GROWTH MECHANISM OF ELECTRODEPOSITED METAL NANOSTRUCTURES

Lauren M. Graham, Doctor of Philosophy, 2014

Dissertation directed by: Prof. Sang Bok Lee

Department of Chemistry & Biochemistry

Electrochemical deposition (ECD) has been a primary method of metal plating for a variety of applications for nearly 100 years. Its popularity is due to its straightforward design, low cost, uniform results, and successful application to a wide range of metals and substrates. Many factors have been shown to influence the composition, texture, and chemical properties of the resultant deposit, such as the current density, the nature and concentration of metal ions, the solution temperature and composition, the applied current waveform, the substrate surface, and agitation. In particular, additives play a complex role in metal deposition due to their ability to greatly alter the growth mechanism and resultant deposit structure. There exists a vast body of work related to the role of additives in various plating solutions, however the majority of investigations on additive effects are focused on planar deposition. For instance, boric acid is a common additive found in nearly all aqueous transition metal plating solutions, yet its influence on metal nanostructure deposition has not been well studied.

In this work, we focus on the impact of additives on the growth of metal nanostructures. Specifically, we investigate the role of boric acid in the ECD of nickel nanotubes (NTs) and nanowires (NWs). First, we demonstrate the difference in the

growth mechanism and nanostructure morphology in the presence and absence of boric acid with electron microscopy and electrochemical analyses. The ECD conditions are modified to further probe the role of boric acid in the 1D growth of nickel nanostructures. The results confirm the function of boric acid in the surface-directed growth of nickel nanostructures. Second, we employ the boric acid-controlled growth mechanism in the synthesis of advanced nickel nanostructures. The potential for the role of boric acid to be applied to the deposition of additional metals is realized through the synthesis of nickel alloy NTs and NWs. Additionally, the advantage of the boric acid-controlled surface-directed growth mechanism is demonstrated through the straightforward synthesis of segmented nanostructures and a 3D interconnected nanotube network.

THE EFFECT OF BORIC ACID ON THE GROWTH MECHANISM OF
ELECTRODEPOSITED METAL NANOSTRUCTURES

by

Lauren M. Graham

Dissertation submitted to the Faculty of the Graduate School of the
University of Maryland, College Park in partial fulfillment
of the requirements for the degree of
Doctor of Philosophy
2014

Advisory Committee:

Professor Sang Bok Lee, Chair
Professor John Cumings
Professor Bryan Eichhorn
Professor Zhihong Nie
Professor Yu-Huang Wang

© Copyright by

Lauren M. Graham

2014

Anyone who has never made a mistake has never tried anything new.

-- Albert Einstein

Dedication

To my parents and my sisters, your endless love and support has meant the world to me and made all this possible.

Acknowledgements

I would first like to thank my advisor, Dr. Sang Bok Lee for his guidance and encouragement over the years, and for always reminding me to consider a problem at its most basic, fundamental level. I am particularly grateful for his understanding and support of my involvement in activities outside of the lab, which allowed me to expand my horizons and develop the nontechnical skills needed to advance my career. I would also like to extend a special thank you to my committee members, Prof. Bryan Eichhorn, Prof. Yu-Huang Wang, Prof. Zhihong Nie, and Prof. John Cumings, for their support and precious time.

Thank you to all of my amazing labmates, both past and present. The Lee lab is without a doubt the best in the department thanks to the support, guidance, and friendship among its members. I have thoroughly enjoyed all of the time we have spent together, in lab and beyond. A special thank you to Thao Liz Nguyen, who took me under her wing and taught me how to be a great grad student while still living life to the fullest. I am honored to be your protégé. Thank you to Dr. Sung Kyoung Kim for sharing your vast knowledge and experience with me, which provided the foundation for this thesis project. I greatly appreciate everything you have shared with me, as a mentor and a friend.

I want to thank Dr. Sz-Chian Liou, Dr. Wen-An Chiou, Dr. Karen Gaskell, and Karthik Sridhara for their assistance in characterizing my nanomaterials. I would like to express my utmost appreciation for Tim Maguel and Jan Endlich, for assisting me in my many EM endeavors and for sharing their infinite EM wisdom. I have enjoyed all over our conversations over the years, both technical and personal, and I hope our paths cross again in the future. Thank you to Natalia White, for being the best lab instructor a TA

could hope for, and for providing me access to instruments and chemicals to tryout several promising (albeit failed) experiments.

A huge thank you goes out to all of my friends, both near and far, for proving that a graduate school acceptance letter is not a death sentence for your social life. Because of you all, I have maintained my sanity through this long and strenuous process. A heartfelt thank you goes out to Dr. Michelle Ward for being an amazing example of a woman who can have and do it all. You have been an exceptional mentor over the years and I am so grateful for your support and friendship.

Above all, I would like to express my appreciation for my amazing family. Without their love and guidance I most certainly would not have made it this far. Thank you for always seeing far greater things in me than I see in myself. I owe my success to your unwavering encouragement and confidence in me.

Table of Contents

Dedication	iii
Acknowledgements	iv
Table of Contents	vi
List of Tables	viii
List of Figures	ix
List of Equations	xii
List of Abbreviations	xiii
Chapter 1: Introduction to the electrodeposition of nanomaterials	1
1.1. Background and motivation	1
1.2. Electrochemical deposition.....	2
1.3. Template materials	5
1.4. Electrolyte composition.....	7
1.4.1. Nickel Electroplating Solutions	8
1.4.2. Other metals	10
1.5. Atomistic growth models for metal deposition	11
1.6. Nanomaterial growth mechanism.....	12
1.6.1. Current proposed nanotube growth mechanisms	13
1.6.1.1. Current-directed growth.....	14
1.6.1.2. Complex formation	16
1.6.1.3. Template modification	18
1.6.1.4. Hydrogen evolution	19
1.6.2. Our proposed mechanism	20
Chapter 2: Borate effect on 1D metal growth.....	22
2.1. Introduction	22
2.2. Experimental method.....	25
2.2.1. Template synthesis of nickel nanostructures	25
2.2.2. Characterization of nickel nanostructures.....	26
2.3. Results and discussion	27
2.3.1. Influence of boric acid concentration on nanostructure morphology .	27
2.3.2. Chronoamperometric analysis	32
2.4. Conclusion	38
Chapter 3: Complexation of nickel-borate to AAO membrane.....	39
3.1. Introduction	39

3.2. Experimental method.....	41
3.2.1. Detection of surface adsorbed solution species	41
3.2.2. Electrodeposition with rinsed AAO templates	42
3.3. Results and discussion	42
3.3.1. Surface adsorption of solution species.....	42
3.3.2. Inhibition of surface complex adsorption	46
3.3.3. Effect of solvent rinsing on nanostructure morphology	51
3.4. Conclusion	54
Chapter 4: Synthesis of advanced nanostructures via boric acid-controlled ECD	55
4.1. Introduction	55
4.2. Experimental method.....	55
4.2.1. Codeposition of nickel alloys.....	55
4.2.2. Synthesis of segmented nickel nanostructures.....	56
4.2.3. Synthesis of 3D nanostructures.....	57
4.3. Results and discussion	58
4.3.1. Nickel alloy nanotubes.....	58
4.3.2. Segmented nickel nanostructures.....	64
4.3.3. Three-dimensional nanostructure network	68
4.4. Conclusion	71
Chapter 5: Summary and Future Work.....	72
5.1. Summary.....	72
5.2. Future Work.....	73
Appendix.....	74
Bibliography	76

List of Tables

Table 4.1 Electrolyte composition for the synthesis of nickel alloy nanostructures. All solutions were prepared in deionized water.....	56
--	----

List of Figures

Figure 1.1	Three-electrode cell for the electrodeposition of 1D nanostructures.	3
Figure 1.2	Schematic of the track-etched synthesis of a PC membrane by the (A) bombardment of heavy ions to form (B) radiation-damaged tracks, which are then (C) etched in a basic solution to form randomly oriented nanochannels. (D) An SEM image showing the top view of a PC membrane.	6
Figure 1.3	Schematic depiction of (A) the growth of nanopores during the anodization of alumina in acidic electrolyte. (B) SEM image of the top view of an AAO membrane..	7
Figure 1.4	Schematic diagram of metal growth under the influence of the tip effect with (A) low current density to form nanowires, and (B) high current density to form nanotubes.	14
Figure 1.5	Schematic diagram of metal growth in the presence of a molecular anchor.	16
Figure 1.6	Schematic diagram of metal growth in the presence of hydrogen evolution.	20
Figure 2.1	Schematic depiction of the general mechanism of nickel deposition.....	22
Figure 2.2	Scheme depicting the complexation of nickel and boric acid	24
Figure 2.3	Deconstructed representation of the working electrode.	25
Figure 2.4	TEM images of nickel nanostructures synthesized from (A, B) standard, and (C, D) boric acid-free electrolyte.	28
Figure 2.5	SEM images of nickel nanostructures synthesized from a solution containing 0.5 M NiSO ₄ and (A) 0.4 M H ₃ BO ₃ , (B) 0.1 M H ₃ BO ₃ , (C) 50 mM H ₃ BO ₃ , and (D) no boric acid. Blue arrows denote nickel NTs, and green arrows denote gold NWs. Scale bar represents 5μm.	30
Figure 2.6	TEM images of (A) nickel NWs synthesized from the boric acid-free electrolyte with (B) a high magnification inset of the NT terminal end from (A).....	30
Figure 2.7	Current transient from the ECD of nickel from the standard electrolyte at -0.2 V, -0.6 V, -0.8V, and -1 V. All depositions were stopped once 4 C of charge had passed. This plot shows the first 33 min of each deposition, however the observed current plateau was maintained until each reaction was terminated.....	31
Figure 2.8	TEM images of nickel NTs synthesized from the standard electrolyte at (A) -0.4V, (B) -0.6V, and (C) -1V.....	32
Figure 2.9	Current transient plots for nickel deposition from the standard and boric acid-free electrolyte.	33
Figure 2.10	Concentration profile of active species that develops over time due to electrochemical consumption at the electrode surface and formation of a diffusion layer.	34
Figure 2.11	Initial portion of the current transient for nickel deposition in the standard electrolyte, highlighting the peak maxima occurring at 18.07 s.	35

Figure 2.12 Non-dimensional i^2/i_m^2 vs. t/t_m transient plot of nickel deposition in the standard electrolyte. Theoretical models for instantaneous and progressive nucleation are shown for comparison.....	37
Figure 3.1 Schematic depiction of nickel-borate adsorption on an AAO membrane. Counter ions have been omitted for simplicity.....	40
Figure 3.2 (A) Full XPS spectra and (B) Ni 2p spectra of an AAO membrane following equilibration in the standard electrolyte, with corresponding (C) data table.....	44
Figure 3.3 (A) Full XPS spectra and (B) Ni 2p spectra of an AAO membrane following equilibration in the boric acid-free electrolyte, with corresponding (C) data table.....	45
Figure 3.4 Chemical structure of a PC membrane.....	47
Figure 3.5 TEM images of nickel NWs synthesized within a PC membrane from the standard electrolyte.....	49
Figure 3.6 XPS spectra of a PC membrane following equilibration in (A) standard and (B) boric acid-free electrolyte, and corresponding (C) data table.....	48
Figure 3.7 (A) TEM and (B) SEM image of nickel NWs synthesized from a solution containing 0.5 M NiSO ₄ , 0.4 M H ₃ BO ₃ , and 0.4 M ethylene glycol.....	50
Figure 3.8 Schematic depiction of the adsorption of the ethylene glycol-borate complex to the AAO surface. Counter ions have been omitted for simplicity.....	50
Figure 3.9 TEM image and corresponding EDS line scan of nickel NTs synthesized from 1 M NaSO ₄ following equilibration in the standard electrolyte and a methanol wash.....	51
Figure 3.10 TEM images of nickel NTs synthesized from a series of (A) 6, (B) 9, (C) 12, (D) 15 equilibration-rinse-electrodeposition cycles.....	53
Figure 3.11 Plot depicting the change in NT wall thickness with successive series of equilibration-rinse-ECD cycles.....	53
Figure 4.1 Voltage profile of a voltage step for the synthesis of branched pores within an AAO membrane.....	58
Figure 4.2 TEM images with corresponding EDS line scans of nickel alloy NTs synthesized from (A) NiFe standard, (B) NiCo standard, and (C) NiFeCo standard electrolytes. Scale bar represents 300 nm.....	60
Figure 4.3 SEM images and corresponding EDS spectra of nickel alloys synthesized from solution (A) NiCo standard, (B) NiFe standard, and (C) NiFeCo standard electrolytes.....	61
Figure 4.4 SEM images and corresponding EDS spectra of nickel alloys synthesized from (A) NiCo BA-free, (B) NiFe BA-free, and (C) NiFeCo BA-free electrolytes.....	63
Figure 4.5 TEM images with corresponding EDS line scans of nickel alloy NWs synthesized from (A) NiFe BA-free, (B) NiCo BA-free, (C) NiFeCo BA-free electrolytes. Scale bar represents 300 nm.....	64
Figure 4.6 TEM images of (A-C) nickel segmented nanostructures synthesized from successive deposition cycles in the standard and BA-free electrolyte. Subsets represent	

high magnification images of individual segments. (D) Table of NT segment lengths corresponding to A-C.....	67
Figure 4.7 SEM images of a 3D nickel nanostructure network synthesized within a homemade 3D AAO template in the standard electrolyte.	69
Figure 4.8 TEM images of nickel nanostructures synthesized from the standard electrolyte with the 3D interconnected AAO template.	70
Figure A.1 XPS spectra and corresponding data table for an AAO membrane following equilibration in deionized water.....	74
Figure A.2 XPS spectra and corresponding data table for an AAO membrane following equilibration in 0.4 M boric acid.....	75

List of Equations

Equation 2.1	Cottrell Equation.	33
Equation 2.2	Theoretical model for the instantaneous nucleation mechanism.	35
Equation 2.3	Theoretical model for the progressive nucleation mechanism.	36

List of Abbreviations

AAO	Anodized aluminum oxide
BA-free	Boric acid-free
c_b	Bulk concentration
ECD	Electrochemical deposition
EDS	Energy-dispersive X-ray spectroscopy
E-R-D	Equilibration-rinse-electrodeposition
HER	Hydrogen evolution reaction
NP	Nanoparticle
NW	Nanowire
PC	Polycarbonate
PEG	Polyethylene glycol
rsf	Relative sensitivity factor
SEM	Scanning electron microscope
3D	Three-dimensional
TEM	Transmission electron microscope
XPS	X-ray photoelectron spectroscopy

Chapter 1: Introduction to the electrodeposition of nanomaterials

1.1. Background and motivation

The hard drive in a laptop is 23 times smaller than that of the first personal computer, yet it can hold 10^5 times the data.^{1,2} The soaring demand for electronic devices with smaller dimensions and enhanced functionality has been a major driving force for the technological advances of the past 30 years. Today's flat screen televisions, cell phones, and mp3 players are all the result of the miniaturization of electronic components. In addition to consumer products, analytical sensors, photonic systems, and medical devices are also experiencing a dramatic reduction in size. As we look to the future, the continued enhancement and miniaturization of these devices will rely heavily on the use of nanomaterial synthesis and processing to generate smaller components with greater capacity.

One class of nanomaterials that holds great promise for applications in all of these fields is one-dimensional metal nanotubes (NTs) and nanowires (NWs). To date, metal NTs and NWs have been utilized in chemical and biochemical sensors,³⁻⁶ photocatalytic reactions,^{7,8} medical diagnostics,⁹⁻¹¹ fuel cells,^{12,13} and data storage devices.^{14,15} In order to incorporate 1D nanostructures into nanoscale devices, reproducible structures must be synthesized in a well-controlled and systematic fashion. The uniformity required for these applications can be achieved using the versatile method of template-assisted electrochemical deposition (ECD).

1.2. Electrochemical deposition

ECD, also referred to as electroplating, is a straightforward method that allows for the high-throughput deposition of a variety of materials. There has been an upsurge in the study of electrodeposition over the last 30 years due to its application in the fabrication of integrated circuits, recording devices, and multilayer structures.¹⁶⁻¹⁸ The low-cost, versatile, and reproducible nature of ECD has helped make it a fixture in the industrial arena. ECD of metals is currently used by numerous industries to impart particular properties onto the substrate. The substrate is often selected for its mechanical properties, and the coating is added to impart properties, such as hardness, corrosion protection, and conductivity, which are lacking in the substrate material.¹⁹ This method has also been used to create zero-, one-, and two-dimensional nanostructures, including nanoparticles (NPs), NWs, NTs, and nanosheets.²⁰⁻²⁸

The fundamental concept of template-assisted ECD makes it an ideal method for the fabrication of 1D nanomaterials. The process follows a bottom-up approach to material synthesis with a nanoporous membrane acting as the template. The typical electrodeposition setup for the synthesis of 1D nanomaterials into a nanoporous membrane, which is shown in Figure 1.1, is performed with a three-electrode cell, which contains a working electrode (cathode), a counter electrode (anode), and a reference electrode connected by a power source. The membrane acts as the working electrode since it is the site of metal reduction. The membrane is first made conductive by sputtering a thin layer of gold onto one side, and then placed in a solution containing the metal ion of interest.

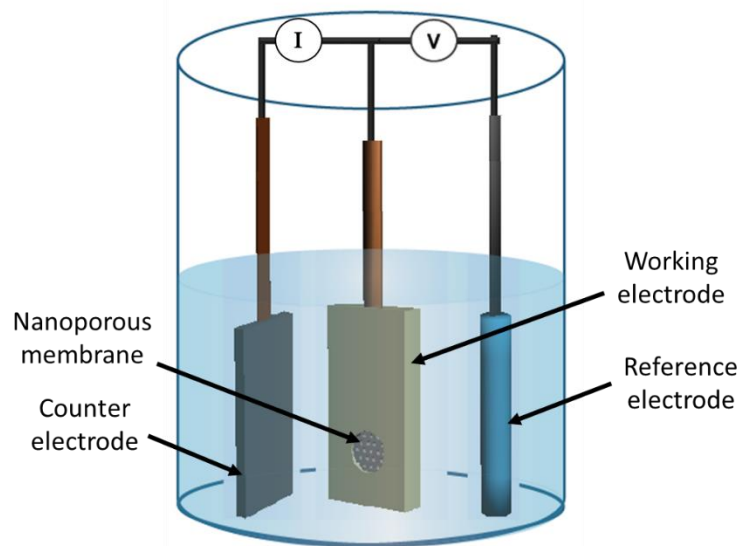


Figure 1.1 Three-electrode cell for the electrodeposition of 1D nanostructures.

When a potential is applied by the power source, the system moves away from the equilibrium potential and the electrodes become polarized. The extent to which the electrode is polarized is referred to as the overpotential. If the overpotential is great enough, an energy transfer occurs between the electrode and the electrolyte species in the form of oxidation-reduction reactions. The reduction of metal ions at the working electrode is balanced by oxidation reactions at the anode. In addition to balancing the charge, the counter electrode is used to measure the current passed during the redox reaction. Conversely, a negligible amount of current is passed through the reference electrode so that a constant potential can be maintained. This allows for a reliable measurement of the overpotential between the working electrode and the reference electrode to be determined.

Although there are many other techniques that are capable of uniform deposition of materials, several disadvantages become apparent when these methods are used for

nanoscale synthesis. For instance, spin-coating and sputtering are primarily thin film techniques designed for planar substrates. During deposition with a nanoporous membrane, the pores of the membrane can be blocked before the entire nanochannel has been coated. Conversely, in ECD, the pores are fully wetted by the electrolyte prior to deposition. As a result, deposition occurs deep into the narrow recesses of nanotemplate, allowing for facile synthesis of NTs and NWs.

Moreover, techniques, such as chemical vapor and atomic layer deposition, indiscriminately coat the entire exposed surface, which does not allow for control over the length of 1D nanostructures. Since ECD is a bottom-up approach, deposition of the material starts at the electrode base and can be stopped at any point to obtain precise control over the length of the resultant NTs/NWs. Furthermore, both methods utilize precursor gas molecules to supply the metal of interest, which are not readily available for all types of metals. On the other hand, ECD is a solution based technique that can be performed under aqueous, organic, acidic, or alkaline conditions. The wide variety of available electrolyte solutions and additives allows for the deposition of nearly any metal.

Finally, ECD is rapid, cost-effective, and environmentally-friendly method with parameters that can be modified to achieve the preferred structure and composition of a material. With the appropriate substrate, solution composition, applied potential, current density, and temperature, precise control over the dimensions, composition, and texture of the deposited material can be achieved.^{14, 29-37} The process often involves less energy and time than many other deposition techniques, which require extremely high temperature and/or pressure, and access to a clean room.

Since variation in any of the aforementioned parameters can significantly impact the resultant electrodeposited material, it is vital that ECD experimental parameters be well controlled. In order to properly select the experimental conditions, one must fully understand the growth mechanism of the material to be deposited. In this thesis, the focus is on the growth mechanism of nickel NTs and NWs. Additionally, the synthesis of iron and cobalt nanostructures are discussed in Section 4.3.1. Specifically, we investigate the impact that the substrate and electrolyte conditions have on the growth of these nanostructures, with the goal of understanding the role of experimental factors on 1D metal growth.

1.3. Template materials

The most common substrates for the ECD of 1D nanomaterials are nanoporous membranes composed of polycarbonate (PC) or anodized aluminum oxide (AAO). PC templates are prepared using the track-etch method, in which high energy, heavy ions penetrate a thin polycarbonate film in order to form radiation-damaged tracks with a diameter of ~10 nm that traverse the organic polymer.^{38,39} The tracks are then etched with a basic solution to form fully developed nanochannels with a diameter controlled by the etching time. Figure 1.2 demonstrates the track-etched synthesis method and the resulting membrane surface.

Since the bombardment of ions determines the concentration and location of the tracks, the nanochannels are randomly dispersed with a pore density of $10^4 - 10^8/\text{cm}^2$. Additionally, the pore axis may be angled up to 20° from the film normal due to the angle of ion incidence.⁴⁰ As a result, the pores can intersect within the film.

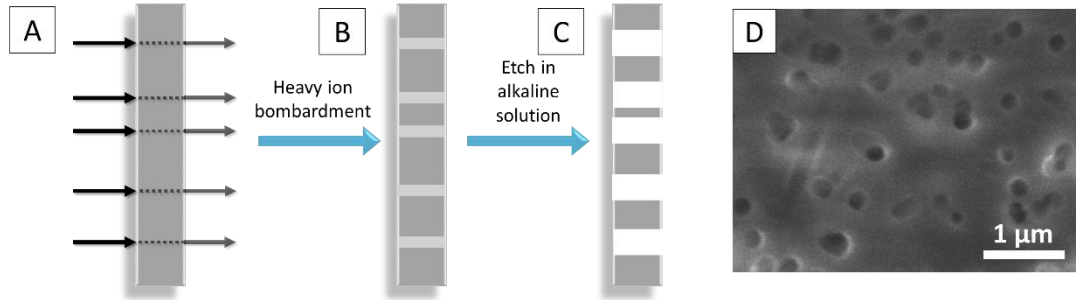


Figure 1.2 Schematic of the track-etched synthesis of a PC membrane by the (A) bombardment of heavy ions to form (B) radiation-damaged tracks, which are then (C) etched in a basic solution to form randomly oriented nanochannels. (D) An SEM image showing the top view of a PC membrane.

While the track-etch method produces randomly oriented pores, the synthesis of AAO is a controlled, systematic process for the production of ordered, monodisperse, cylindrical pores. AAO is formed through the anodization of pure aluminum in acidic or basic solution. Figure 1.3A illustrates the process that occurs during anodization. The applied potential ejects aluminum ions from the metal towards the electrolyte and oxygen species from the electrolyte toward the metal, which results in the formation of an alumina (Al_2O_3) surface layer. A hexagonal array of pores with a pore density of 10^{10} pores/ cm^2 develops in the alumina as a result of the anodization process (Figure 1.3B).⁴¹⁻
⁴³ The distance between the pores, known as the cell size, is determined by the applied voltage, and the length of the pores is directly proportional to the anodization time. Whereas the pore diameter, which can range from 5 - 400 nm, is controlled by the composition, temperature, and duration of anodization, along with the pore widening step.^{42, 44, 45}

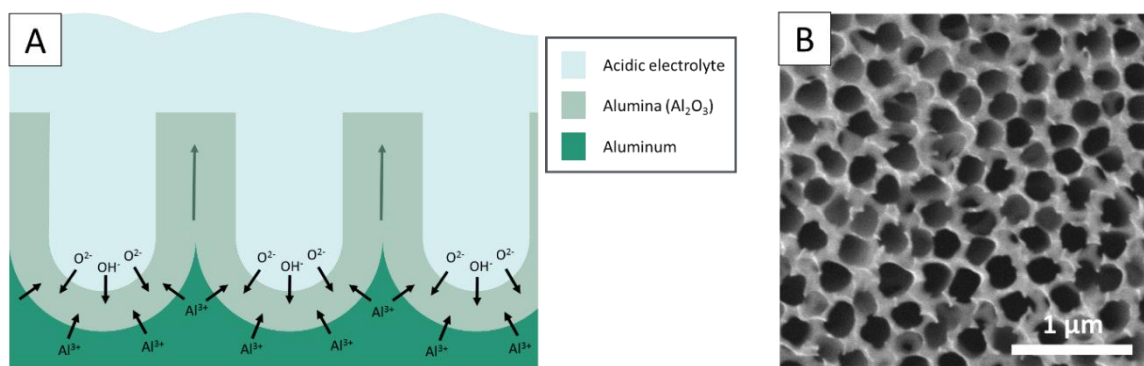


Figure 1.3 Schematic depiction of (A) the growth of nanopores during the anodization of alumina in acidic electrolyte. (B) SEM image of the top view of an AAO membrane.

Initially the pores develop in a random fashion, and then become ordered as the anodization process continues. As a result, AAO templates are often prepared using a two-step anodization process. The alumina film produced during the first anodization is chemically etched, leaving behind scalloped edges where the pores resided. During the second anodization, the pores grow from the scalloped edges to produce AAO with uniform pores oriented perpendicular to the template normal forming a template with long-range order. Due to its enhanced uniformity, our work primarily utilizes AAO. However, ECD with PC membranes is described in Section 3.3.2 as a way to demonstrate the importance of certain chemical properties of the nanoporous membrane during metal ECD.

1.4. Electrolyte composition

The electrolyte composition is another parameter that significantly impacts the ECD deposit. The basic components of an electroplating solution are the metal ions of interest, an acid or alkali, and one or more additives to improve the quality of the deposit. Typically, sulfate and/or chloride salts are used in acid solutions, whereas cyanide salts are used in basic solutions. Due to the complex influence of additives, there have been

countless investigations into the mechanism of action of ions, molecules, and complexes in various electroplating baths.^{35, 46-55}

In general, additives can be classified into three categories: levelers, brighteners, and surfactants. Levelers are additives that cause a thicker deposit to form in the recesses of the substrate, compared to the peaks and edges, in order to achieve a smoother, more even deposit surface. Additives that produce finer deposits are referred to as brighteners since the resulting material is capable of reflecting more visible light due to a smaller crystal structure. Finally, surfactants are surface-active agents, typically anionic or non-ionic compounds that reduce the surface tension and allow the substrate to be more easily wetted. In addition to these effects, the presence of additives can impact many other factors of ECD, such as current efficiency and surface adsorption. In this section, we review the various electrolyte compositions common to nickel deposition and the effect they have on the deposition process. We also highlight popular electrolyte compositions for the ECD of other important metals.

1.4.1. Nickel Electroplating Solutions

Nickel is a highly versatile element that is extensively used in a range of industrial applications for its high strength, magnetic coercivity, corrosion- and oxidation-resistance. As a result, the ECD conditions and the growth mechanism for nickel deposition have been studied in detail.^{29, 35, 37, 47, 51, 52, 56-61} The most common nickel plating solutions are based on the Watts bath, which contains nickel sulfate and nickel chloride as Ni²⁺ suppliers and boric acid as a buffer. Changes to the deposit structure are seen with variations in the concentration of these components and in the additives selected, as described below.

For instance, Holm and O'Keefe demonstrated that an unbuffered (i.e. boric acid free) nickel sulfate solution produced a dark, brittle deposit due to the precipitation of nickel hydroxide on the substrate surface.⁶² In order to improve the deposit appearance, the activity of nickel must be increased, either by increasing the nickel concentration or temperature, or decreasing the solution pH. Similar results were found with deposition from unbuffered nickel chloride solutions, in which flaky, high stress nickel deposits were formed.⁵⁹

In the presence of boric acid, however, the appearance of the nickel deposit was greatly improved. Instead of a brittle, irregular surface, a smooth, glassy nickel surface is formed with boric acid. The improved surface structure has been attributed to the buffering ability of boric acid.^{34, 51, 63, 64} Further improvements were made by Mockute et al. using three additives: saccharin, 2-butyne-1,4-diol, and phthalimide.⁵³ Saccharin and butynediol are well known brighteners for nickel ECD.^{29, 65, 66} Collectively, saccharin and 2-butyne-1,4-diol produce a bright deposit with small crystal size and low internal stress. The addition of phthalimide further enhances the levelling and brightening capability, and increases the hardness of the deposit.⁵³ A multitude of other organic additives have been studied with the nickel chloride and/or sulfate bath, including thiourea, coumarin, p-toluene sulfonamide, naphthalene trisulfonate, benzene sulphonate, and pyridine.^{29, 35, 52, 66, 67}

Alternative nickel sources have also been studied. For instance, nickel sulfamate has been combined with nickel chloride for the high speed production of low internal stress, ductile nickel deposits. Tsuru et al. showed that the effects of boric acid in a sulfamate bath are comparable to the Watts bath, with an observed buffering ability at the

electrode surface.⁶⁸ As the boric acid concentration decreased, the pH near the electrode quickly increased from 4 to 5.75, while the current efficiency gradually decreased from 100% to 63%. Additionally, the change in boric acid concentration caused an increase in internal stress which led to the formation of cracks in the nickel film. During the high speed deposition, passivation of the nickel anode occurred, which resulted in an increased deposition potential, sulfamate decomposition, and pH fluctuations. To prevent passivation and promote dissolution of the anode, halide ions are often added to the sulfamate solution.³⁵

1.4.2. Other metals

In addition to nickel, there is a variety of electrolyte compositions for the ECD of other metals. Here, we briefly review electroplating solutions for several metals that are popular in industrial applications. Copper is a widely popular coating that is used in electrical, automotive, and aerospace industries for its ductility, adhesion, corrosion-resistance, and electrical and thermal conductivity. Copper is typically deposited using the sulfate or cyanide salt in acidic or alkaline solutions, respectively.⁶⁹⁻⁷³ Due to its popularity, a great deal of research has been focused on the influence of additives in copper electroplating solutions. Common additives for copper ECD include chloride, polyethylene glycol, thiourea, dextrin, and fluoroborate.^{46, 71, 74}

Metal coatings are also used for aesthetic purposes in which case the color and brightness of the material are of significant importance, along with its adhesion to the substrate. Chromium is often used to coat decorative pieces, such as faucets and lighting fixtures. The electrolyte solutions for chrome plating are fairly simple. Typically they contain chromic acid and a small amount of sulfate.⁷⁵ However, the addition of fluoride

anions, such as fluoride, fluoroborate, and silicofluoride, has shown to increase the efficiency of the deposition process.

In addition to pure metal coatings, alloy deposits can be achieved with ECD. For instance, lead-tin coatings, which are used in printed circuit boards, are prepared with a single solution containing the both metal salts. The composition of the resulting alloy depends on factors such as the molar ratio of lead:tin, the presence of additives, current density, and solution temperature.⁷⁶ Up until the 1980's lead-tin electroplating solutions were based on fluoroborate compounds, however they have widely been replaced by methanesulfonate solutions.⁷⁶⁻⁷⁹ Typically, solutions also contain an aromatic aldehyde or ketone as a brightener, and a surfactant, such as Triton-X, peptone, and proprietary compounds.^{78, 80-82}

Regardless of the metal, the composition of an electrolyte plays a substantial role in the process of ECD. Any modification to the contents of the solution can greatly impact the appearance and properties of the resultant deposit. Therefore, a thorough understanding of the effect of all solution contents on the growth mechanism is fundamental to successful ECD.

1.5. Atomistic growth models for metal deposition

A description of the growth mechanism of metal deposition has been evolving for nearly 85 years. The first theoretical explanation of the electrodeposition growth process was developed by Erdey-Gruz and Volmer in 1930.^{83, 84} It was assumed that the substrate surface was perfectly smooth. Therefore a nucleation step was required in order for metal growth to occur. By the late 1940's, it had been determined that the surface

contained microscopic imperfections, which act as growth initiation sites.^{85, 86} As a result of this finding, several modified growth mechanisms were proposed, most notably by Bewick,⁸⁷ Armstrong and Harris,⁸⁸ and Scharifker and Hills.⁸⁹

To this day, the nucleation and growth models continue to evolve with the advancement of technology. Through the use of powerful analytical instruments, a more in-depth investigation into the electrodeposition process is attainable. For instance, surveys of the surface morphology with the scanning tunneling microscope and the atomic force microscope have greatly improved the understanding of the atomic processes that occur as a material is deposited.⁹⁰⁻⁹³ From these studies it is known that voltage, solution pH, and temperature greatly affect the crystallinity, alloy composition, and surface morphology of the deposited material.

1.6. Nanomaterial growth mechanism

As focus shifts from the deposition of planar coatings to micro- and nanostructures, a new understanding of the factors controlling the atomic process within the small, confined pores of nanotemplates becomes significant. Therefore, a thorough investigation into the growth mechanism of metals within nanoporous templates is vital to the future of ECD. While the above models provide great insight into the deposition onto planar surfaces, they fail to adequately describe the chemical and physical processes occurring within the nanoporous template during nanowire and nanotube synthesis. At the nanoscale, factors such as substrate morphology, additive effects, and applied potential have an amplified effect on the structure and composition of the resultant deposit, compared to macroscale growth. Therefore, novel mechanisms must be

presented to explain the growth of nanomaterials within the confined spaces of nanoporous templates.

In this section, we address the main NT growth mechanisms that have proposed to date. Although a variety of theories have been presented to describe the growth of metal NTs, we focus on four of the most prevalent proposed mechanisms: current-directed growth, complex formation, template modification, and hydrogen evolution.

1.6.1. Current proposed nanotube growth mechanisms

The growth mechanism of NTs is particularly intriguing since growth across the nanochannel does not occur in a uniform fashion, as it does with planar and nanowire growth. Instead, the growth rate is significantly faster along the pore wall, compared to the central pore region. In the past 20 years, numerous growth mechanisms have been suggested for the template synthesis of metal nanotubes that describe the role of various experimental conditions on the resultant morphology. The basis for electrochemical nucleation and growth rely on the interplay between growth kinetics and thermodynamics. When the growth rate parallel to the pore wall is greater than the perpendicular growth rate (i.e. $v_{\parallel} > v_{\perp}$), nanotube formation is observed.⁹⁴⁻⁹⁷ However a complete understanding of the growth process of nanomaterials within a nanoporous template has been hampered by the difficulty of direct, in-situ observation.

In this section, four main proposed nanotube growth mechanisms will be discussed. Each mechanism provides detailed insight into the growth of metal nanotubes at the atomic level. Although these mechanisms are presented individually, they are not mutually exclusive. As previously discussed, metal deposition is a complex process,

which is easily affected by a wide array of variables. Therefore, when analyzed thoroughly, it is possible to attribute the resultant morphology of electrodeposited metal nanostructures to a contribution of two or more mechanisms.^{25, 54, 58, 94-104}

1.6.1.1. Current-directed growth

According to the current-directed mechanism two key factors determine the morphology of 1D metal nanostructures: the electrode surface morphology and the current density. The electrode surface of a nanoporous template is formed by sputtering gold, or an alternative conductive metal, on the bottom of the template. During the sputtering process, metal atoms penetrate and deposit up to several hundred nanometers into the pore, forming an annular shaped electrode. When a potential is applied, the sharp curvature of the electrode leads to a greater accumulation of charge at its tip (i.e. along the pore wall). A higher charge density means the tip of the annular electrode is more electrochemically active than the remaining area. This phenomenon, which is referred to as the ‘tip effect’, causes the electrode tip to be the preferential site of metal nucleation and deposition.^{15, 95, 102, 105, 106} Therefore, deposition is more likely to occur at the pore wall compared to the central region and to result in the formation of NTs, as depicted by Figure 1.4 B.

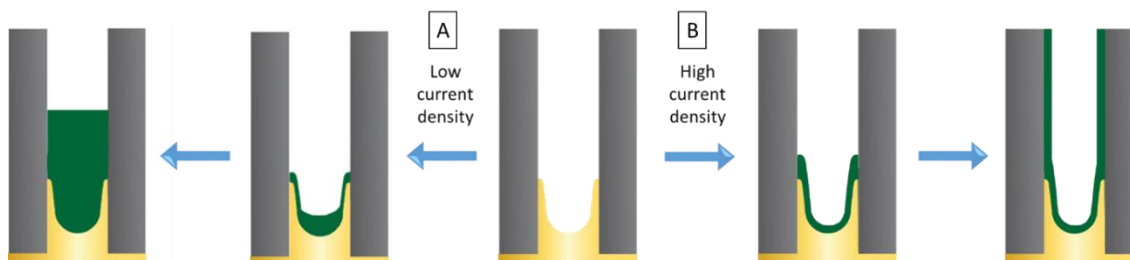


Figure 1.4 Schematic diagram of metal growth under the influence of the tip effect with (A) low current density to form nanowires, and (B) high current density to form nanotubes.

In addition to electrode morphology, current density plays a significant role in controlling the morphology of 1D nanostructures by altering the competitive growth rates, v_{\parallel} and v_{\perp} . When a high current density is applied, a large potential gradient is formed and the tip effect is intensified.^{94, 96} As deposition continues, a dynamic deposition interface and a dynamic metal ion diffusion layer develop and move with the growing NT.¹⁰⁷ The metal ion concentration below the deposition interface becomes significantly low due to ion consumption at the interface.

Current density is a measure of the rate of an electrochemical reaction, so a high current density ensures that the deposition rate will be significantly faster than the metal ion diffusion rate into the pore. As a result, the concentration of metal ions cannot be replenished and deposition within the pore center is negligible. Conversely, low current density has little effect on v_{\parallel} and v_{\perp} , and the slower deposition allows bulk metal ions to diffuse into the entire length of the pore to overcome the tip effect. Deposition then occurs uniformly across the entire pore to form NWs, as depicted by Figure 1.4 A.

The effect of current density has also been described in terms of a critical deposition potential at which point $v_{\parallel} \approx v_{\perp}$.⁹⁷ Ohm's law states that current density is directly proportional to the applied electric field. Therefore, if the applied potential does not surpass the critical threshold, the reaction rate is slow and thermodynamics control the deposition process. Consequently, 2D plane growth occurs across the entire pore ($v_{\parallel} < v_{\perp}$) to form NWs. Alternatively, at potentials greater than the critical potential, kinetics control the deposition process so that propagation up the pore wall occurs faster than axial growth ($v_{\parallel} > v_{\perp}$), which leads to the formation of NTs.

1.6.1.2. Complex formation

The mechanism of complex formation has been studied in detail for the planar deposition of metals, yet few studies relate its effect to NT/NW growth. In general, a chemical species capable of acting as a molecular anchor is added to the electrolyte. The additive adsorbs to the cathode surface and complexes with metal ions in solution, which significantly increases the metal ion concentration at the cathode surface, as shown in Figure 1.5. As a result, the rate of metal reduction along the pore wall is greater than that in the center void.^{46, 108, 109}

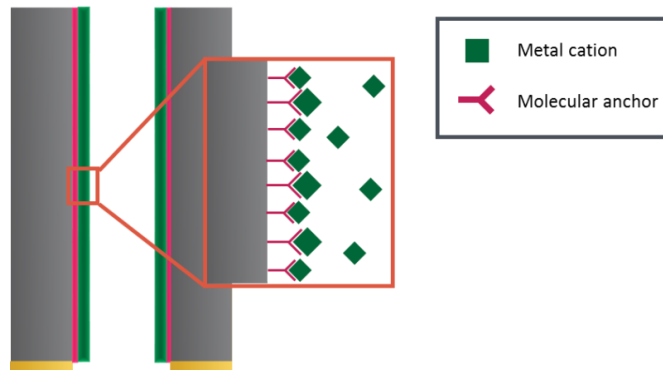


Figure 1.5 Schematic diagram of metal growth in the presence of a molecular anchor.

Some molecular anchors not only increase the metal ion surface concentration but are also capable of accelerating the rate of electron flow from the electrode to the metal ion. Such additives are referred to as ion-bridging compounds. For example, thiocyanate, a common electroplating additive, has been shown to increase the rate of deposition for transition metals due to ion-bridging.¹⁰⁹

To further understand complex formation and its effect on electrodeposition, we consider the influence of polyethylene glycol (PEG) and Cl^- on Cu deposition.

Considerable attention has been paid to the effect of additives on copper electroplating solutions since copper deposition is utilized for numerous industrial applications, such as corrosion protection and electronic connectivity. Raman spectroscopy has shown that adsorption of PEG and Cl^- to a copper substrate occurs to a greater extent when both additives are present in solution.¹¹⁰⁻¹¹³ For instance, Feng et al. used Raman studies and modelling calculations to determine that the surface complex involved a three-coordinate Cu atom with one Cl^- and two ether oxygen atoms from the PEG chain acting as ligands.¹¹⁰

An in-depth analysis on the influence of these additives by Bonou et al. established that the PEG:Cu:Cl complex does not exist in solution since the diffusion rate of Cu to the cathode was not affected by the incorporation of PEG and/or Cl^- .⁷⁴ This study also revealed that the presence of both additives altered the Cu deposition mechanism.⁷⁴ Cyclic voltammograms of electrolyte containing Cu only, Cu with Cl^- , and Cu with PEG show an intersection of the anodic and cathodic current. It is well known that such a crossover indicates the formation of metal nuclei on the electrode.^{31, 74, 114} When both additives were present in solution, no crossover was observed which signifies that the surface-bound complex inhibits nucleation and significantly influences the deposition mechanism.

Chowdhury et al. demonstrated that the surface adsorption of the PEG:Cu:Cl complex had a significant impact on the morphology of electrodeposited 1D copper nanostructures.⁵⁴ Solid Cu nanowires were synthesized from electrolytes containing Cu, Cu with PEG, and Cu with Cl^- . However, the presence of both PEG and Cl^- in solution led to the formation of Cu nanotubes. Additionally, nanotube growth has been shown to

occur via complex formation without the use of additives. Immobilization of the metal ion at the template surface can occur through direct interaction with the surface groups. Tourillon et al. postulated that the synthesis of cobalt (or iron) nanotubes was the result of the electrostatic interaction between Co^{2+} (or Fe^{2+}) ions and the $-\text{CO}_3^{2-}$ moieties of the polycarbonate membrane.¹¹⁵

1.6.1.3. Template modification

In a process that resembles complex formation, the pore walls of the nanoporous template is chemically modified to ensure an increased metal ion concentration along the pore wall. The template surface is functionalized with a molecular anchor prior to ECD. Equilibration of the template in the plating solution generates a high concentration of metal along the cathode surface. As a result, an increased rate of reduction is observed when a potential is applied.

Template modification is one of the oldest known mechanisms for nanotube electrodeposition. In fact, the first demonstration of template-assisted electrochemical synthesis of metal nanotubes by Brumlik and Martin was achieved by functionalizing an AAO membrane with organocyanide groups, which acted as a molecular anchors for the gold ions in the plating solution. The interaction of gold with the surface groups lead to a thin coating of gold ions along the pore wall.²⁵ When the appropriate potential was applied the increased concentration of gold led to preferential deposition along the pore wall, which ultimately generated gold nanotubes. In the absence of the organocyanide, gold deposition within unmodified AAO formed solid gold nanowires. In a similar fashion, AAO templates have been functionalized with organoamines, and PC templates with vinyl triethoxylated silane in order to synthesize nickel nanotubes.^{58, 100}

Electroless deposition has also been used to decorate the pore walls with conductive nanoparticles for enhanced deposition at the pore surface.¹⁰¹ Rather than increase the concentration of the metal ion, the nanoparticles provide a conduction path for the current to travel along the insulating AAO surface. As with organic functionalization, the use of conductive nanoparticles results in an increased rate of deposition along the pore wall to form nanotubes.

1.6.1.4. Hydrogen evolution

Hydrogen evolution is known to accompany the electrochemical deposition of many transition metals, including nickel, iron, and cobalt. It has been hypothesized that nanotube growth is the result of a combination of hydrogen evolution and gas bubble suppression.^{30, 104, 116} The hydrogen evolution reaction (HER) can be broken down into 4 steps: (1) diffusion of H_3O^+ to the cathode, (2) desolvation and partial reduction of H_3O^+ at the cathode to form chemisorbed hydrogen ($\text{M-H}_{(\text{ads})}$), (3) formation of $\text{M-H}_{2(\text{ads})}$ either through the combination of two $\text{M-H}_{(\text{ads})}$ hydrogen atoms, or of a $\text{M-H}_{(\text{ads})}$ with a proton and electron, and (4) desorption and diffusion of molecular hydrogen as a gas bubble.¹¹⁷

During electrodeposition within a template, the final step is hindered by the nanoscale dimensions of the pores. Gas bubble formation is suppressed until supersaturation of hydrogen is reached inside the pore.¹⁰⁴ The confined dimensions of the pore force the bubble to expand along the pore axis as the HER produces more hydrogen at the deposition interface, only desorbing and diffusing into the bulk when it reaches the pore opening. Therefore, the generation of hydrogen obstructs the central pore region and restricts metal deposition to the pore wall, as shown in Figure 1.6.

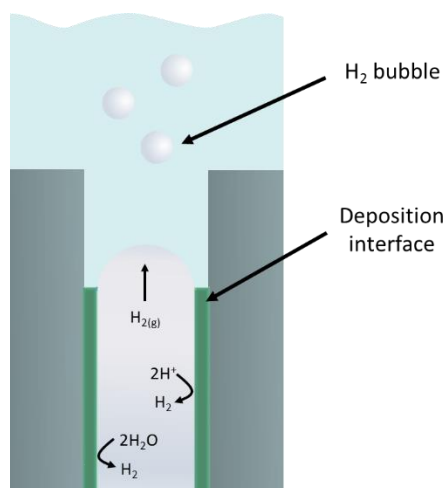


Figure 1.6 Schematic diagram of metal growth in the presence of hydrogen evolution.

For some transition metals, the hydrogen can act as a mild reducing agent which also enhances nanotube deposition. For instance, Liu and Park demonstrated that adsorbed hydrogen was a contributing factor in the formation of palladium nanotubes.³³ Under the acidic conditions of PdCl₂ plating solution, the AAO template developed a positive charge due to the protonation of surface hydroxyl groups. A diffusion layer containing negatively charged Pd(II)-Cl complexes was formed in order to maintain electroneutrality. Since the concentration of Pd at the template surface was distinctly higher than the bulk solution, the rate of Pd deposition was greater along the pore wall. Additionally, the reduced hydrogen that formed as a result of the applied potential adsorbed to palladium via an exothermic process and aided in the reduction of Pd(II) which enhanced $v_{||}$.^{118, 119}

1.6.2. Our proposed mechanism

In this work, we investigate the growth mechanism of nickel NTs in the absence of physical modifiers, such as annular electrodes and template modification. We present evidence for a surface-directed growth mechanism controlled by the adsorption of a

nickel-borate complex to the template surface. In Chapter 2, we investigate the impact of boric acid on the morphology of the resulting nickel nanostructures. Electrochemical analysis is also presented in order to explain the role of boric acid in nickel deposition. In Chapter 3, the impact of the template surface chemistry on the deposition of NTs versus NWs is investigated. Based on the data presented, a novel NT growth mechanism is introduced, which relies on the adsorption of the nickel-borate complex to achieve surface-directed growth. Chapter 4 presents advanced electrodeposition experiments that are possible due to the surface-directed growth process.

Chapter 2: Borate effect on 1D metal growth

2.1. Introduction

The deposition of nickel onto planar substrates, such as nickel, copper and platinum, has been described in detail.^{29, 35, 37, 48, 50, 51, 53, 56, 59, 68, 120, 121} The established mechanism is depicted in Figure 2.1. A complex between a Ni^{2+} ion and an anion, proven to be Cl^- or OH^- , forms in solution. When the complex adsorbs to the electrode surface, two consecutive one-electron transfer reactions occur which reduce the nickel ion and release the anion.

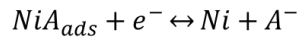
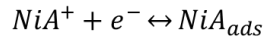
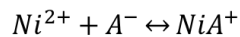


Figure 2.1 Schematic depiction of the general mechanism of nickel deposition.

Despite the consensus regarding the general mechanism of nickel deposition, there is continued research into the role of additives, particularly of boric acid. Boric acid is a well-known additive that has been used in the ECD of a wide variety of metals, including nickel, cobalt, iron and zinc.^{34, 64, 122-126} As discussed in Section 1.4, additives play a significant role in the determination of the metal deposit texture, which is the non-random orientation and distribution of crystallites. Amblard proposed that the competitive growth rates between various nuclei control the orientation of growth crystallites, and ultimately the resultant deposit texture.²⁹ The kinetics of this competition is primarily controlled by the solution pH and the cathodic reaction.

Therefore, many metal electroplating solutions, including the Watts bath, require the presence of a buffer to maintain the solution pH at the electrode during ECD.^{51, 127} When the overpotential of metal ion reduction is greater than that of proton reduction, hydrogen evolution is observed in conjunction with metal deposition. As a result, protons are readily consumed at the cathode, which significantly increases the pH at the electrode surface and decreases the current efficiency. During nickel deposition, the rise in pH results in the precipitation of nickel hydroxide on the cathode, thereby passivating the surface and inhibiting further deposition.^{48, 120} When HER occurs in conjunction with nickel deposition, the resultant deposit typically appears dark, glassy, and flaky.^{51, 59, 62, 68,}

128

Conventionally, boric acid has been added to nickel electroplating solutions to prevent surface passivation and generate smooth deposits by acting as a proton-donating buffer capable of maintaining the pH at the electrode surface. Ji et al. demonstrated that a lower pH was maintained at the electrode surface during nickel deposition when boric acid was present in the electrolyte.¹²⁷ As a result, the texture of the electrochemically deposited nickel was enhanced and a smooth deposit was formed.^{29, 61, 129, 130}

Since the pKa of boric acid is 9.2, it cannot effectively buffer in the pH range of acidic nickel electroplating solutions by simple proton dissociation. Therefore, Durose proposed that the buffer capacity arose from the polymerization of boric acid molecules.^{50, 131} It was later determined that the buffering of nickel solutions below pH 5 was the result of the complexation of nickel and two boric acid molecules.^{57, 132} Figure 2.2 shows that the complexation results in the release of two protons. Moreover, it has been observed that nickel preferentially complexes with boric acid over hydroxyl ions,

which acts to stabilize nickel ions and to limit the possibility of Ni(OH)₂ precipitation.^{48,}

133

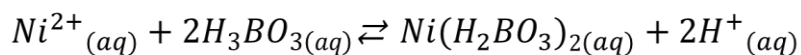


Figure 2.2 Scheme depicting the complexation of nickel and boric acid

In addition to buffer capacity, emerging evidence indicates that boric acid also acts as a homogeneous catalyst for metal deposition.^{60, 61, 134} Numerous studies report that the adsorption of boric acid on the cathode surface shifts the overpotential and inhibits nucleation of nickel ions, leading to smoother, more refined deposits.^{51, 120, 135, 136} It has also been suggested that the adsorption of boric acid reduces the available surface area for proton reduction.^{135, 136} Despite the evidence that boric acid alters the deposition of nickel, a well-defined mechanism has yet to be proposed to support the claims. Furthermore, the role of boric acid on nickel ECD has yet to be extended beyond the study of planar deposition.

Herein, we present the investigation of the impact of boric acid on the deposition of nickel nanostructures within an AAO template. We demonstrate that boric acid alters the deposition mechanism presented in Figure 2.1, which significantly influences the resultant nanostructure morphology. In the following chapter we describe a mechanism to support the findings presented here. In order to focus our investigation solely on the influence of boric acid on nickel deposition we utilized flat-top base electrodes in lieu of annular electrodes in all of our electrodeposition experiments. The flat-top electrodes eliminated the tip effect which has been cited as a primary factor in NT versus NW growth.

2.2. Experimental method

2.2.1. Template synthesis of nickel nanostructures

Nickel nanostructures were synthesized using commercial AAO membranes (Whatman) with a pore diameter of 200 nm and a membrane thickness of 60 μm . One side of the membrane contained uniform, parallel pores, and the opposite side, referred to as the branched side, contained randomly interconnected pores. A Denton Vacuum Desktop III was used to sputter a gold layer (ca. 100 nm) onto the branched side in order to generate a conductive surface for electrodeposition. Following the sputtering process, the working electrode was assembled, as shown in . Copper tape was attached to the gold side of the AAO membrane to provide an electrical contact for the working electrode. The AAO was sandwiched between two silicon spacers and two pieces of Teflon with an electroactive window of 0.1 cm^2 that exposed the non-branched side of the AAO.

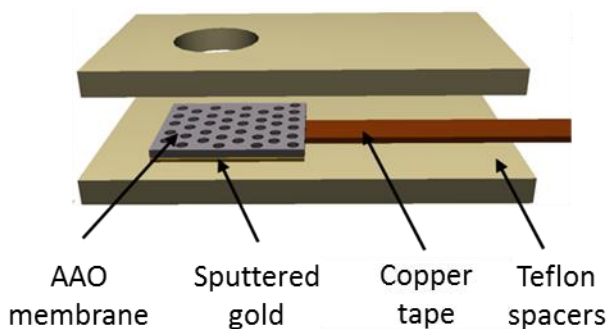


Figure 2.3 Deconstructed representation of the working electrode.

All electrochemical experiments were carried out with a VSP Modular Potentiostat/ Galvanostat by Bio-Logic Science Instruments using a three-electrode cell setup with a platinum foil counter electrode and an Ag/AgCl reference electrode. Unless otherwise stated, all potential measurements were recorded with respect to the reference electrode. Prior to all electrodeposition experiments, the working electrode was

sonicated in the electrolyte to ensure proper wetting of the template pores. Gold NWs were electrochemically deposited from a commercial gold plating solution (OROTEMP 24) under a constant current of -0.3 mA for 30 minutes and used as flat-top base electrodes for nickel deposition. Unless otherwise stated, nickel was deposited from the standard aqueous electrolyte, which contained 0.5 M NiSO₄, 0.4 M H₃BO₃, at a constant potential of -1V until 4 C of charge had passed. Sodium sulfate was added to boric acid-free (BA-free) solutions in order to achieve a high conductivity comparable to the standard electrolyte.

2.2.2. Characterization of nickel nanostructures

The morphology of the nickel nanostructures was investigated with a field emission scanning electron microscope (SEM; Hitachi S-4700) operated at 5 kV, and a field emission gun transmission electron microscope (TEM; JEOL JEM 2100F) operated at 200 kV. For SEM analysis, the gold side of the membrane was attached to a specimen mount with carbon tape. The AAO membrane was dissolved in 3 M NaOH for 30 min and rinsed several times with water. For TEM analysis, the sputtered gold layer was removed by mechanical polishing to allow for the liberation of free-standing nanostructures. The AAO was dissolved in 3 M NaOH and the solution was rinsed with water until a neutral pH was achieved. The nanostructures were then dispersed in ethanol and a 7 μ L sample was dropped onto a formvar/carbon-coated copper TEM grid.

2.3. Results and discussion

2.3.1. Influence of boric acid concentration on nanostructure morphology

Nickel was electrochemically deposited from solutions containing 0.5 M NiSO₄ and a range of boric acid concentrations. According to Figure 2.4, well-defined NTs with a hollow center and uniform wall thickness of 12 nm were formed from the standard electrolyte. This immediately suggests a surface-mediated growth mechanism may be dominant here, as the growth begins from a flat topped Au electrode. The structure of the NTs that originated from the base of the AAO template displayed branched junctions due to the interconnected pore network of the template. Despite the abrupt change in template geometry, the hollow NT structure was maintained throughout the entire branched section. The complete and uniform deposition of nickel within the branched pores indicates that the electrochemical growth occurred in a more complex manner than a simple 1D direction. Based on these results, we propose a surface-directed growth mechanism controlled the ECD of nickel in the standard electrolyte.

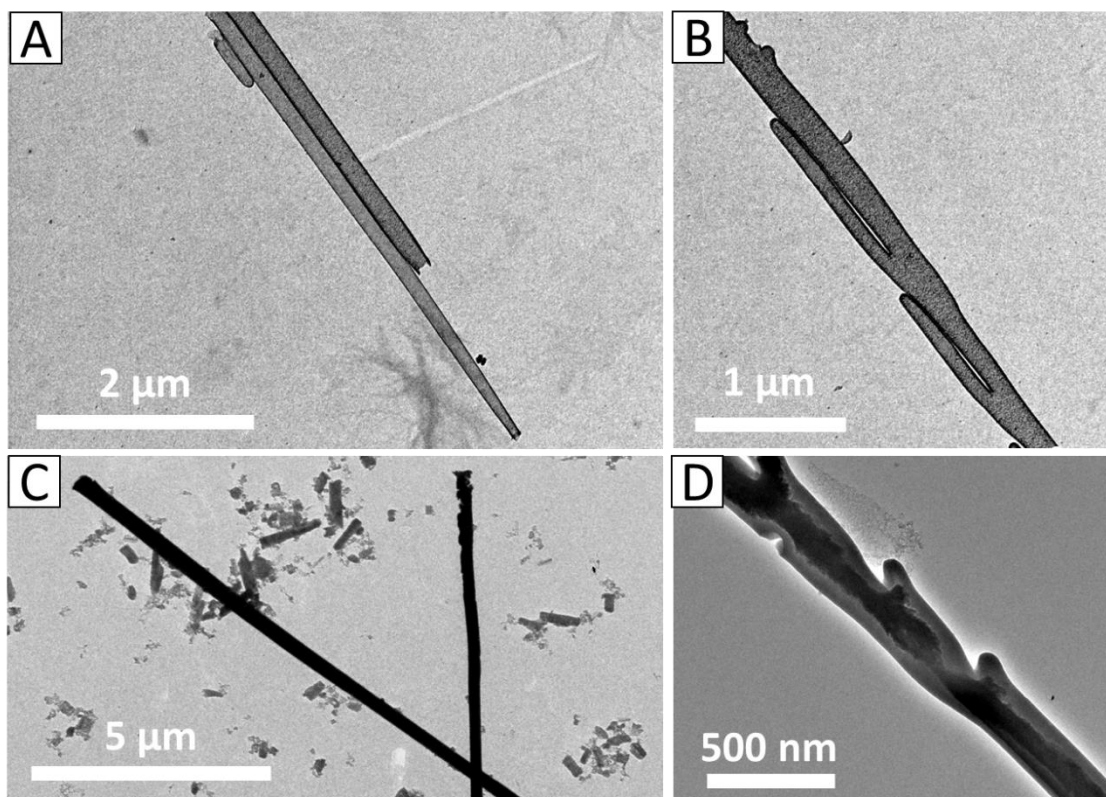


Figure 2.4 TEM images of nickel nanostructures synthesized from (A, B) standard, and (C, D) boric acid-free electrolyte.

In contrast, deposition of nickel in the absence of boric acid resulted in NWs. Unlike the structures synthesized from the standard electrolyte, fully developed NW branches were not evident in the BA-free samples. Several small protrusions can be seen on the NW in Figure 2.4, which indicates the initial site of NW branching. However, the deposition was terminated at the pore junction, preventing the development of a fully branched region. The lack of defined branched NWs signifies that the electrochemical growth occurred in a 1D manner with no indication of surface-directed growth. As the nickel was deposited up the template pore, the branched junction became blocked, which prevented further deposition into the depths of the branched region.

These results demonstrate the influence that boric acid has on the electrochemical growth and resultant morphology of nickel nanostructures. Further evidence was observed by studying the morphology as a function of the boric acid concentration. The SEM images in Figure 2.5 illustrate the effect that the boric acid concentration had on the structural integrity of the nanostructures. As the concentration of boric acid decreased, an increase in rigidity was observed. As shown above, the standard electrolyte (0.4 M boric acid) generated uniform NTs. The thin walls and large aspect ratio of the NTs caused them to collapse and form a NT film over the gold NWs when the AAO template was removed.

As the concentration of boric acid decreased to 0.1 M and 50 mM, an increase in the rigidity of the deposited nanostructures was observed. Figure 2.5 B and C show the structures from the NT film that begin to stand upright. This is likely due to a thickening of the NT walls or a change in hardness of the deposited nickel. Finally, electrodeposition from a BA-free electrolyte produced rigid nickel NWs capable of remaining fully erect without the support of the template. Despite the open ended nanostructures seen in Figure 2.5, TEM analysis revealed that fully-filled NWs with NT tips on the terminal end were synthesized from the BA-free electrolyte (Figure 2.6).

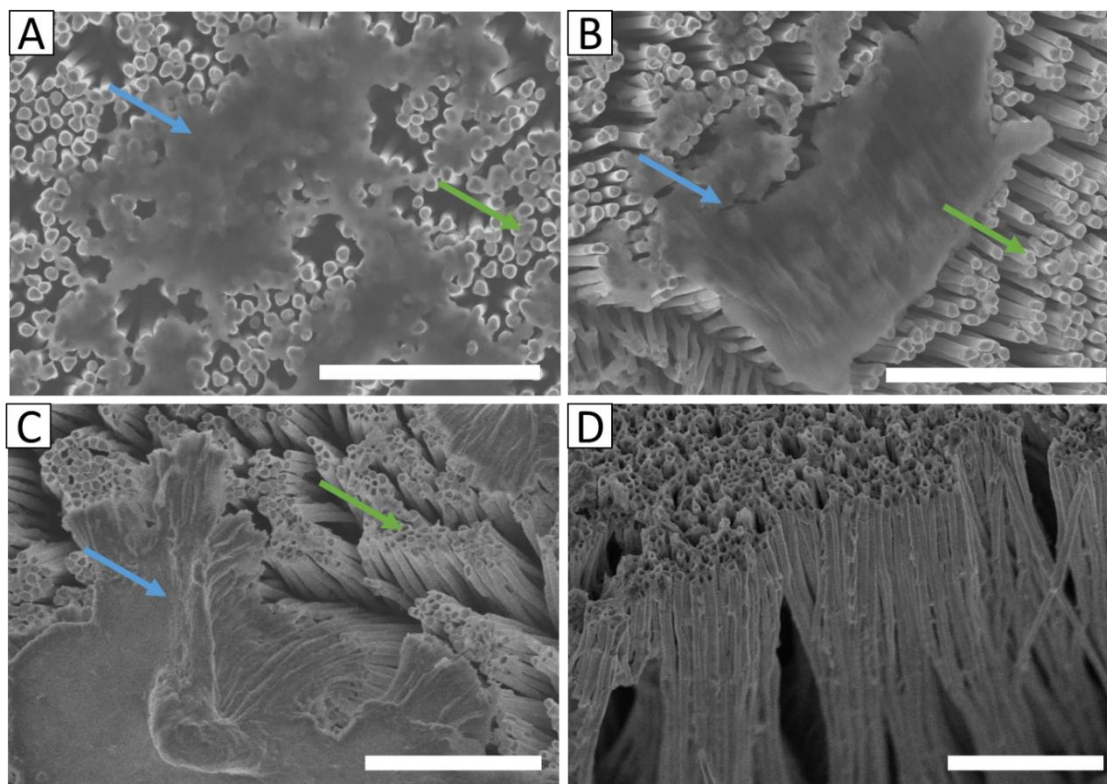


Figure 2.5 SEM images of nickel nanostructures synthesized from a solution containing 0.5 M NiSO₄ and (A) 0.4 M H₃BO₃, (B) 0.1 M H₃BO₃, (C) 50 mM H₃BO₃, and (D) no boric acid. Blue arrows denote nickel NTs, and green arrows denote gold NWs. Scale bar represents 5 μm.

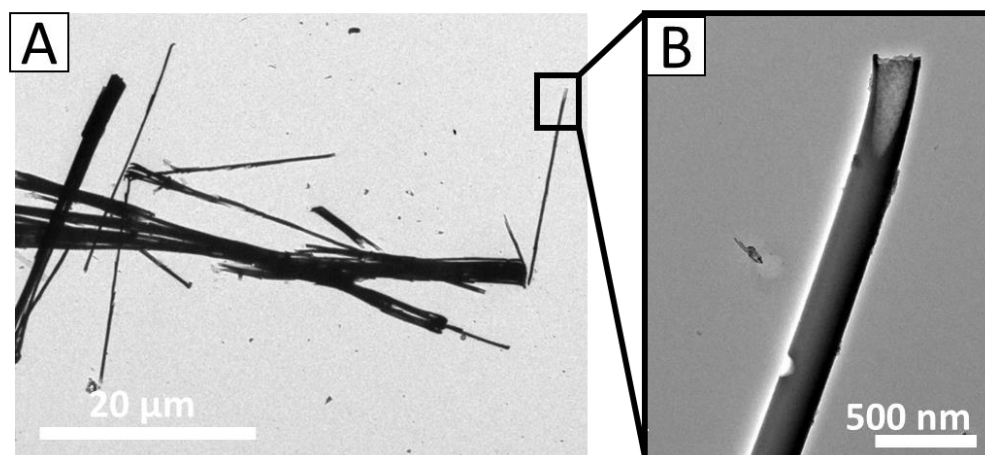


Figure 2.6 TEM images of (A) nickel NWs synthesized from the boric acid-free electrolyte with (B) a high magnification inset of the NT terminal end from (A).

In order to confirm that the current-directed growth mechanism did not play a role in the synthesis of the NT structure, nickel was potentiostatically deposited from the standard electrolyte at a variety of current densities. The current density was modified by adjusting the magnitude of the applied potential, as shown by the current transients in the Figure 2.7. In order to allow for comparison among deposits, the deposition was stopped after 4 C of charged had passed, which correlated to a 30 min deposition at -1 V. Previous reports that cited the tip effect as the controlling factor in NT growth demonstrated that a reduction in potential as small as 0.2 V altered the growth mechanism and resulted in NW formation.^{96, 97, 106} Figure 2.8 demonstrates that NTs were synthesized even at low current densities, where the current-directed mechanism predicts NW growth. The current-directed growth mechanism relies on the presence of the tip effect, which was eliminated in our experiments by the flat-top base electrodes.

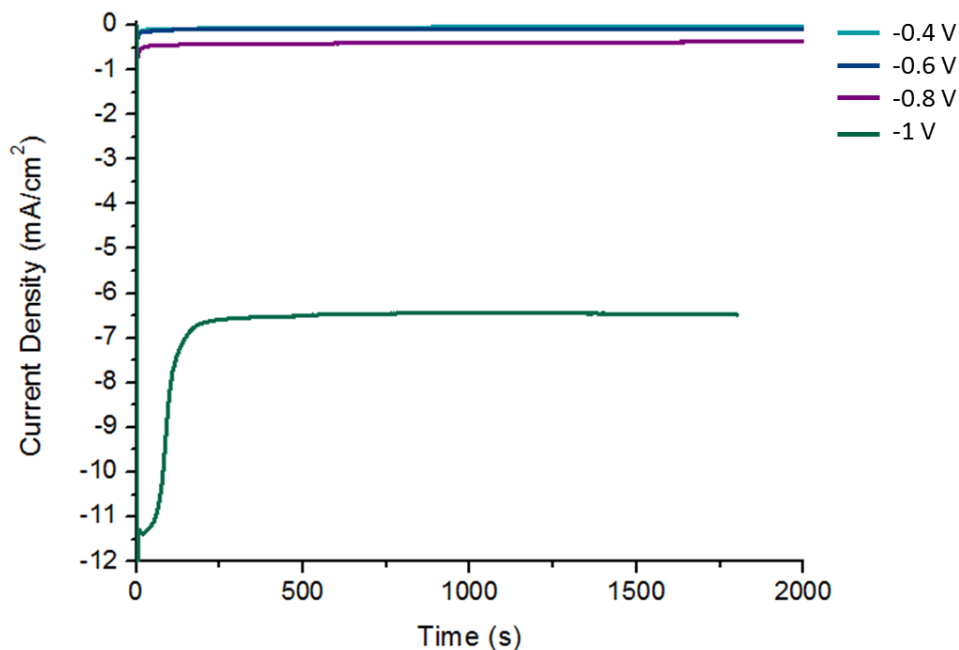


Figure 2.7 Current transient from the ECD of nickel from the standard electrolyte at -0.2 V, -0.6 V, -0.8V, and -1 V. All depositions were stopped once 4 C of charge had passed. This plot shows the first 33 min of each deposition, however the observed current plateau was maintained until each reaction was terminated.

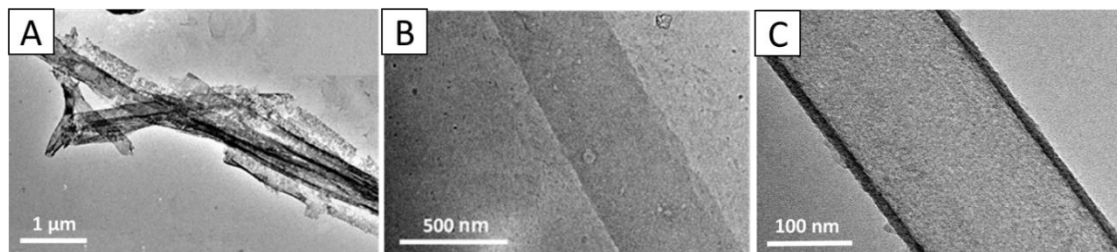


Figure 2.8 TEM images of nickel NTs synthesized from the standard electrolyte at (A) -0.4V, (B) -0.6V, and (C) -1V.

Therefore, we attribute the growth of NTs versus NWs to the presence and absence of boric acid, respectively. These results indicate that boric acid not only acts as a buffer but also significantly influences the ECD of nickel. The presence of boric acid alters the nickel deposition mechanism and allows for the surface-directed growth of nickel NTs.

2.3.2. Chronoamperometric analysis

The effect of boric acid on the deposition mechanism was further studied using chronoamperometry. Chronoamperometry is an electrochemical analysis technique performed under potentiostatic conditions. In a typical chronoamperometric analysis, the current response of the working electrode is monitored following the application of a potential step. The results are then displayed in the form of a current transient, which illustrates the aggregate change in electrode current due to the various processes occurring during deposition. In this work, the potential was stepped from the open circuit potential ($\sim +0.26$ V) to the deposition potential (-1V).

Figure 2.9 shows the potentiostatic current transients from the nickel deposition in the standard and BA-free electrolyte. The current response from the BA-free electrolyte shows a severe decrease during the initial 5 seconds of deposition, which can be

attributed to the double layer charging brought on by the potential step.^{89, 137-139} The remaining transient exhibits traditional Cottrell behavior, signified by an exponential decay described by Equation 2.1. This monotonic decrease in current is in accordance with the concentration profile of active species near the electrode surface.

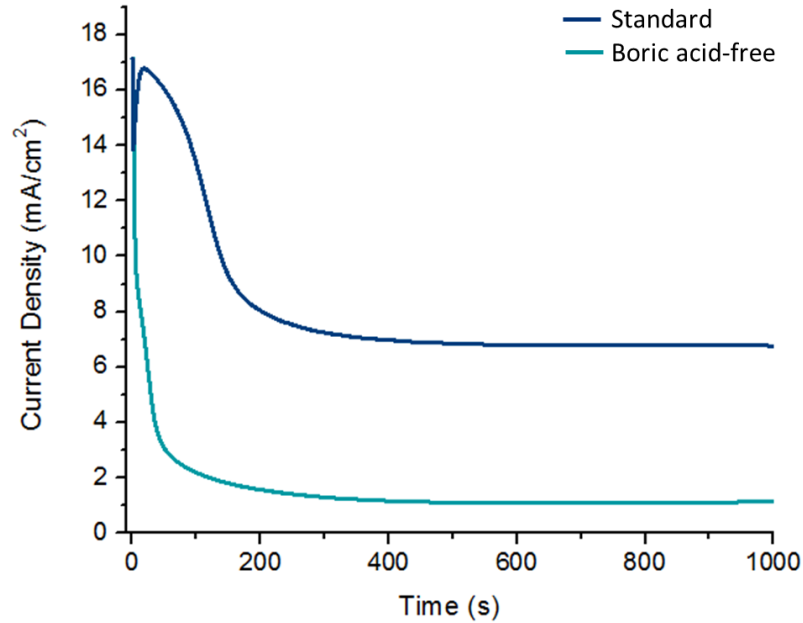


Figure 2.9 Current transient plots for nickel deposition from the standard and boric acid-free electrolyte.

$$i = \frac{nFAC\sqrt{D}}{\sqrt{\pi t}}$$

Equation 2.1 Cottrell Equation.

Prior to the potential step, the concentration of nickel ions at the electrode surface was equal to the bulk concentration (C_b). At the onset of the potential step, the nickel ions at the surface were reduced. Further reduction of nickel required diffusion of bulk species to the electrode. As the deposition process continued, the diffusion layer gradually expanded into the bulk solution until the system reached steady state, as shown

in Figure 2.10. Under steady state conditions, the current was limited by the mass transport of nickel ions to the electrode surface, and is denoted by a plateau in the current transient.

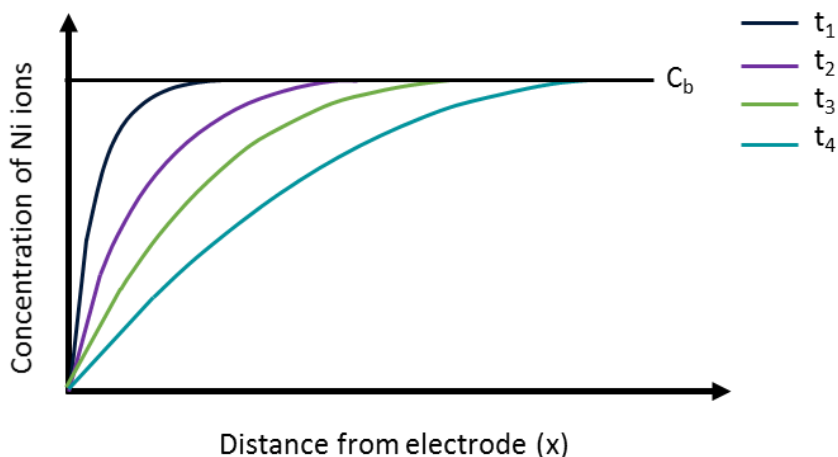


Figure 2.10 Concentration profile of active species that develops over time due to electrochemical consumption at the electrode surface and formation of a diffusion layer.

In comparison, the current transient from the deposition in the standard solution shows a well-defined peak. From Figure 2.11, it is clear that the dramatic current decrease due to double layer charging was still present. However, following this decrease the current rose to a maximum before exponentially decaying. Finally, the current plateaued at the steady state current when the reaction reached diffusion control. The presence of a current maxima has long been viewed as an indication of a nucleation mechanism.^{31, 32, 74, 89, 128, 138, 140} The increase in current arises due to an increase in the active surface area brought on by the crystal growth at the various nucleation sites. This is consistent with our expectation that surface mediated growth of nanotubes would result in an expanding active surface area along the tube walls.

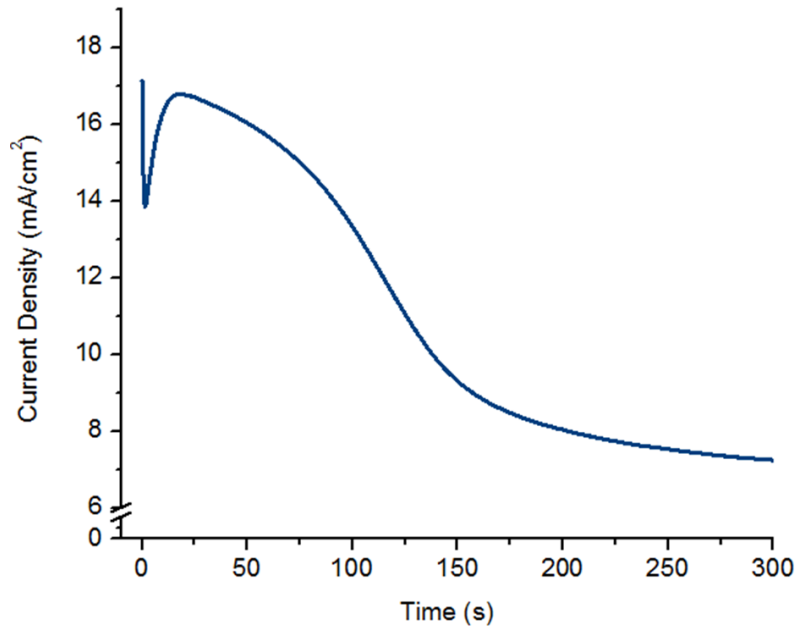


Figure 2.11 Initial portion of the current transient for nickel deposition in the standard electrolyte, highlighting the peak maxima occurring at 18.07 s.

In order to analyze the nucleation process, the data was compared to the two theoretical models derived by Scharifker and Hills.⁸⁹ The first model describes the instantaneous nucleation mechanism. Instantaneous nucleation corresponds to the immediate activation of all nucleation sites at the onset of the potential step. In contrast, the progressive model describes the situation in which the nucleation sites become active as deposition proceeds. The instantaneous and progressive nucleation processes are represented by Equation 2.2 and Equation 2.3, respectively.

$$\frac{i^2}{i_m^2} = \frac{1.9542}{t} \left[1 - e^{-1.2564 \left(\frac{t}{t_m} \right)^2} \right]$$

Equation 2.2 Theoretical model for the instantaneous nucleation mechanism.

$$\frac{i^2}{i_m^2} = \frac{1.2254}{\frac{t}{t_m}} [1 - e^{-2.3367(\frac{t}{t_m})^2}]$$

Equation 2.3 Theoretical model for the progressive nucleation mechanism.

Initially, the data closely followed the response predicted by the instantaneous nucleation model, as shown in Figure 2.12. This indicates that, following the application of the potential step, nucleation occurred quickly and all at once. However, at longer times, both models predict a drastic decrease in current, which denotes the terminated nucleation process due to the overlap of diffusion zones and active species concentration depletion. The non-dimensional transient for the deposition of nickel from the standard electrolyte shows only a modest decrease in current that continues until the limiting current is reached. The elevated current, compared to the theoretical models, indicates a higher concentration of nickel ions at the electrode surface than predicted by a simple diffusion model. These results suggest that boric acid influences the nickel ion concentration at or near the template surface. In Chapter 3, we further investigate the effect of boric acid on the surface nickel concentration.

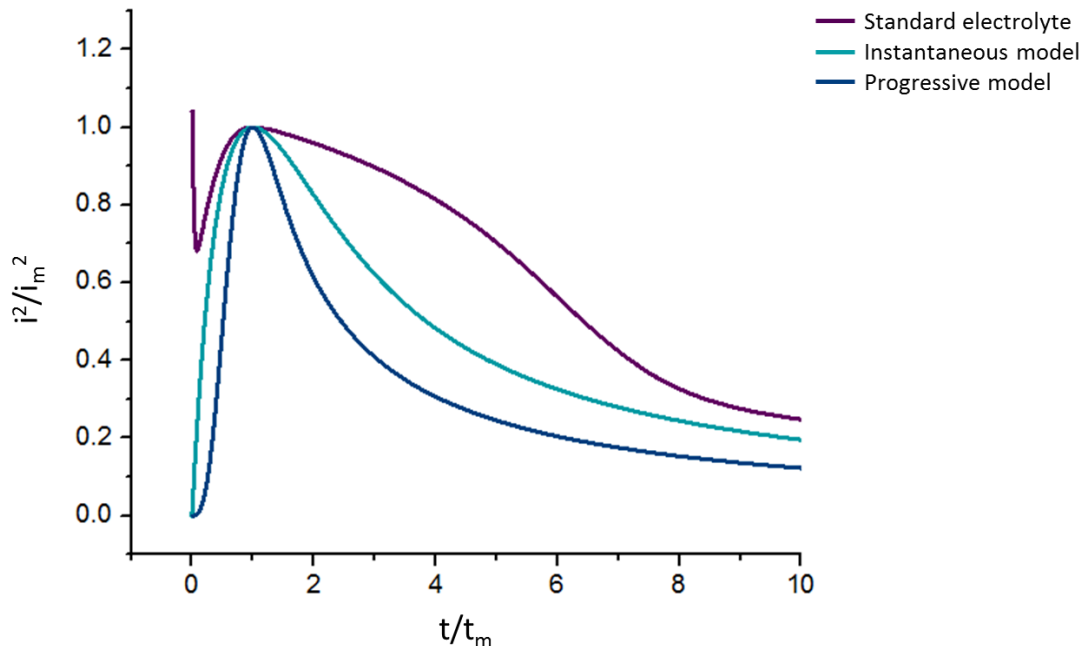


Figure 2.12 Non-dimensional i^2/i_m^2 vs. t/t_m transient plot of nickel deposition in the standard electrolyte. Theoretical models for instantaneous and progressive nucleation are shown for comparison.

The difference in current transients provides key evidence to the influence of boric acid on the mechanism of nickel ECD. Whereas, the monotonic decrease observed in the absence of boric acid is characteristic of Cottrell behavior, the presence of a current maxima in the presence of boric acid denotes a nucleation-based mechanism.¹⁴⁰ Additionally, the concentration of nickel at the electrode surface appears to be higher than expected in the presence of boric acid. The limiting current in the standard electrolyte is 6 times higher than that of the BA-free electrolyte. Since the limiting current is a mass transfer-controlled process, we can deduce that nickel ions are more readily available at the electrode surface in the standard electrolyte. This is consistent with strong surface interactions mediating the mechanism. Although it is not possible to fully understand the growth mechanism by analysis of the current transient alone, these

results demonstrate a clear difference in deposition mechanisms between the two electrolytes, due to the presence or absence of boric acid.

2.4. Conclusion

It is widely accepted that the planar deposition of nickel occurs through two consecutive one-electron transfer mechanisms that are mediated by a nickel-anion complex, and that additives greatly affect the resultant morphology of the deposit. In this chapter, we demonstrated the significant impact of boric acid on the morphology of the deposited nanostructure. Based on TEM and SEM images, we conclude that boric acid plays a role in controlling the ECD of nickel NTs versus NWs. Through electrochemical analyses we were able to observe the fundamental differences in the growth mechanism. Both the microscopy images and electrochemical analysis indicate a surface-mediated growth process for the ECD of nickel in the standard electrolyte. In the following chapter, we propose a mechanism to explain the effect of boric acid on the electrochemical growth of nickel nanostructures that allows for such observations.

Chapter 3: Complexation of nickel-borate to AAO membrane

3.1. Introduction

The conventional view of the role of boric acid adsorption in the nucleation and planar deposition of nickel was addressed in Chapter 2. In this chapter we present a novel mechanism of action for boric acid adsorption and its impact on the ECD of nickel nanostructures. We propose that the surface-mediated growth of nickel NTs in the standard electrolyte was achieved due the adsorption of the nickel-borate complex to the pore wall of the AAO template. It is well known that boric acid binds to hydroxyl-containing compounds with high affinity. This interaction has been employed in the molecular recognition, separation, and transport of carbohydrates for over 50 years.¹⁴¹⁻¹⁵⁰

The interaction of boric acid with hydroxyl moieties extends to heterogeneous reactions with metal oxide surfaces. Numerous studies have shown the ability of boron species to adsorb to metal oxide surfaces, specifically aluminum and iron oxides, in aqueous solutions.¹⁵¹⁻¹⁵⁹ Reported logarithmic values for the surface complexation constant of boric acid absorption onto alumina, which range from 4.1-4.83, indicate high affinity of the alumina surface for boric acid.^{153, 154} Su and Suarez demonstrated the presence of both the trigonal planar and tetrahedral boric acid species on the surface of amorphous aluminum and iron hydroxides.¹⁵⁵ Peak et al. revealed the complex chemistry behind the interaction of hydrous iron oxide and boric acid with attenuated total reflectance FTIR.¹⁵¹ Although it was not possible to determine an exact complexation mechanism, it was suggested that a monodentate complex initially formed through an outer-sphere interaction between borate and a surface hydroxyl group. The

loss of a proton or water molecule then resulted in the formation of an inner-sphere bidentate complex.

From this data, it can be inferred that boric acid readily binds to the alumina surface of the AAO template. Due to the high concentration of both nickel and boric acid in Watts-type plating solutions, and the knowledge that nickel-borate is a prominent species in such solutions, we propose that boric acid binds to the AAO surface as the nickel-borate complex.^{51, 60, 127, 132} Figure 3.1 shows the mono- and bidentate surface species of the nickel-borate complex that are predicted to be present on the template surface based on spectroscopic analysis of boron surface species.^{153, 155} Furthermore, we propose that the presence or absence of the surface-bound complex acts as a determining factor in the synthesis of NTs and NWs, respectively.

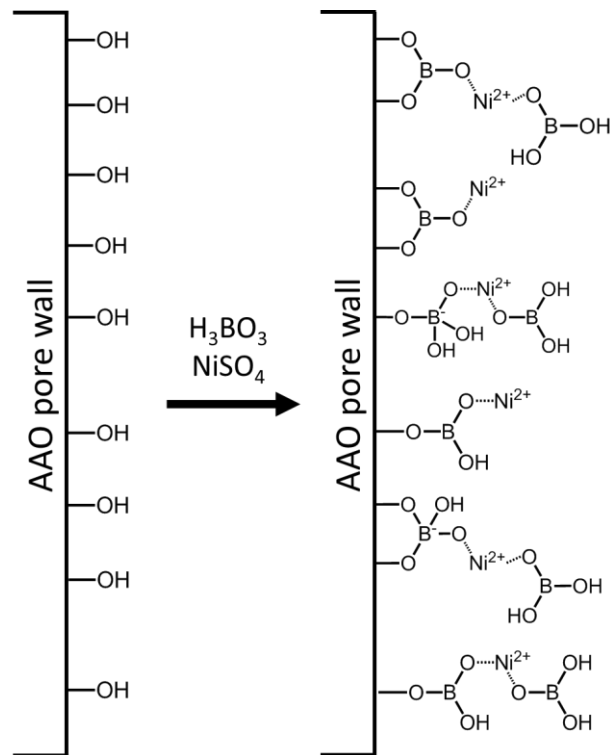


Figure 3.1 Schematic depiction of nickel-borate adsorption on an AAO membrane. Counter ions have been omitted for simplicity.

The adsorbed complex facilitates the surface-directed growth of nickel nanotubes by modifying the concentration of nickel ions in the proximity of the pore walls. Considering the surface hydroxyl concentration of alumina typically ranges from 3 to 15 OH/nm², the adsorption of nickel-borate to hydroxyl moieties can substantially increase the nickel concentration at the template surface, compared to the bulk solution.^{33, 160-163} The localized concentration of nickel results in enhanced deposition along the pore wall to generate nickel nanotubes. This mechanism is similar to the complex formation mechanism presented in Section 1.6.1.2. However, the boric acid-mediated mechanism allows for controlled NT growth without any additional molecular anchor.

Herein, we provide data to support the proposed mechanism for the adsorption of the nickel-borate complex and its influence on the growth of nickel nanostructures. Specifically, we show that nickel adsorption on the AAO surface occurs to a greater extent when boric acid is present in the solution. Additionally, we demonstrate that the ECD of nickel NTs requires the presence of both boric acid and template surface hydroxyl moieties.

3.2. Experimental method

3.2.1. Detection of surface adsorbed solution species

The presence of adsorbed species on the AAO template was analyzed with x-ray photoelectron spectroscopy (XPS). Commercial AAO membranes were immersed in standard electrolyte (0.5 M NiSO₄, 0.4 M H₃BO₃) and BA-free electrolyte (0.5 M NiSO₄, 0.06 M NaSO₄), and allowed to equilibrate for 5 min. Solutions of pure deionized water,

and 0.4 M boric acid were used as controls (see Appendix). The AAO was removed and washed with methanol to remove unbound species. XPS measurements were performed on a Kratos AXIS 165 spectrometer.

3.2.2. Electrodeposition with rinsed AAO templates

Electrodeposition was performed as described in Section 2.2.1 with some modifications. Briefly, flat-top gold NWs were deposited within the pores of the exposed AAO of the working electrode. The working electrode was equilibrated in the standard electrolyte for 10 minutes, thoroughly washed with methanol, and then equilibrated in methanol for 3 minutes. The electrode was placed in a 1 M sodium sulfate solution, along with a platinum counter electrode and Ag/AgCl reference electrode. Nickel was electrodeposited at -1 V for 10 min. Characterization of the resulting nanostructures was performed as described in Section 2.2.2.

3.3. Results and discussion

3.3.1. Surface adsorption of solution species

The first step in validating the nickel-borate surface-directed growth mechanism was to confirm the increased concentration of adsorbed nickel on the AAO surface in the presence of boric acid. The adsorbed species were detected by XPS. XPS is a valuable method of surface analysis due to its ability to detect all elements with an atomic number of 3 or higher that are present in the top ca. 10 nm of a material. The chemical and electronic state of the elements in a material are determined by measuring the number and kinetic energy of ejected electrons following irradiation with an x-ray beam. Each element emits a unique set of electrons with characteristic binding energies, which allows

for elemental analysis. The elemental composition of a material is presented as a percentage, which is calculated by dividing the measured signal intensity by the relative sensitivity factor (RSF), and normalizing the results.

Figure 3.2 and Figure 3.3 show the full XPS spectra and the Ni 2p spectra of an AAO membrane after equilibration in the standard and BA-free electrolyte, respectively. The ratio of Ni:Al was analyzed in order to compare the degree of nickel adsorption between the two solutions. For the standard electrolyte sample the Ni:Al ratio was 0.056, whereas the ratio for the BA-free sample was 0.035. Therefore, the concentration of adsorbed nickel was 1.6 times greater following equilibration in standard electrolyte, compared to the BA-free solution.

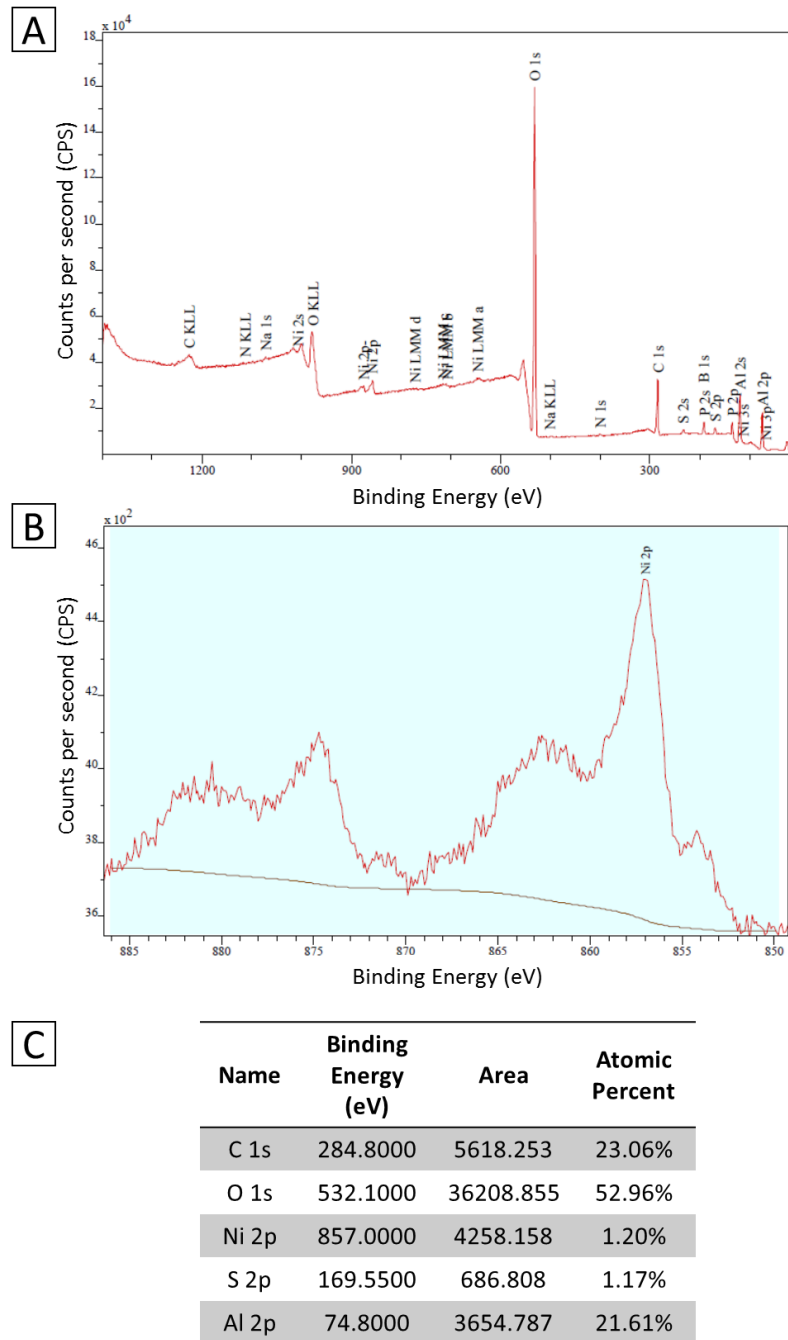


Figure 3.2 (A) Full XPS spectra and (B) Ni 2p spectra of an AAO membrane following equilibration in the standard electrolyte, with corresponding (C) data table.

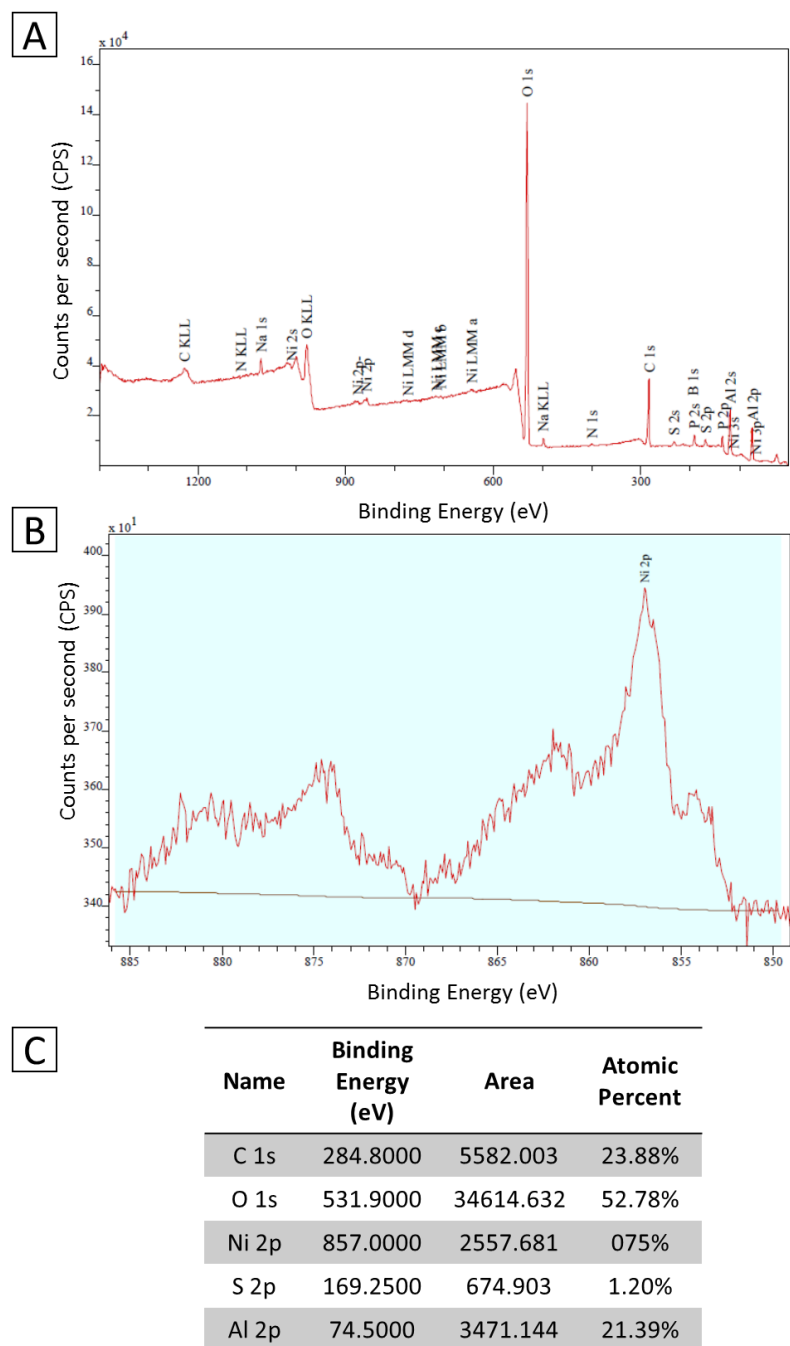


Figure 3.3 (A) Full XPS spectra and (B) Ni 2p spectra of an AAO membrane following equilibration in the boric acid-free electrolyte, with corresponding (C) data table.

From these results, we conclude that boric acid enhanced nickel adsorption to the AAO surface through the binding of the nickel-borate complex, as shown in Figure 3.1.

The small nickel signal detected in the BA-free sample was due to the direct interaction of nickel with the metal oxide surface. It is well known that transition metals, including nickel, adsorb to metal oxides in aqueous solution.¹⁶⁴⁻¹⁶⁷ However, the low signal intensity indicates that the nickel - alumina interaction was not as favorable as the interaction between boric acid and the alumina surface. In the standard electrolyte, nickel was affixed to the surface through the nickel-borate complex. The stable interaction between borate and the oxide surface allowed the complex to remain bound to the AAO following the methanol wash.

3.3.2. Inhibition of surface complex adsorption

In order to demonstrate the role of nickel-borate adsorption onto the template surface in the growth mechanism of nickel NTs, the ECD conditions were modified in such a way as to inhibit the formation of the surface complex. This was achieved through two methods: (1) the use of a template lacking surface hydroxyl groups, and (2) the addition of a competitive binder to the electrolyte. In the first method, a PC membrane was used as a template in place of AAO. The PC membrane is a porous polymer membrane composed of bisphenol carbonate monomers, shown in Figure 3.4. The absence of surface hydroxyl moieties was confirmed with XPS analysis by Latella et al.¹⁶⁸ As expected, C=O and C-O bonds from the carbonate species was detected on the surface PC substrates. However, hydroxyl groups were only detected after a water-plasma pre-treatment was performed.

XPS analysis by Latella et al. demonstrated the absence of hydroxyl moieties on the surface of PC substrates. As expected, only C=O and C-O bonds from the carbonate species was detected on the PC substrates. It should be noted that phenolate moieties

form on the nanochannel surface during the track-etch processing of the PC membrane. However, XPS analysis revealed that nickel was not present on the PC membrane surface following equilibration in the standard and BA-free electrolyte, as shown in Figure 3.. Therefore, it was concluded that no significant interaction occurred between the PC surface and nickel-borate complex.

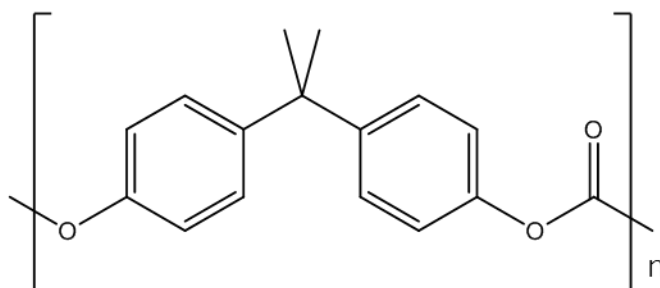


Figure 3.4 Chemical structure of a PC membrane.

As a result, the use of a PC template resulted in the ECD of NWs from the standard electrolyte (Figure 3.). The absence of sufficient surface hydroxyl moieties on the PC template prevented the nickel-borate complex from interacting with the template surface. Without a disproportionate nickel ion concentration within the pore, deposition occurred uniformly across the entire nanochannel to form NWs.

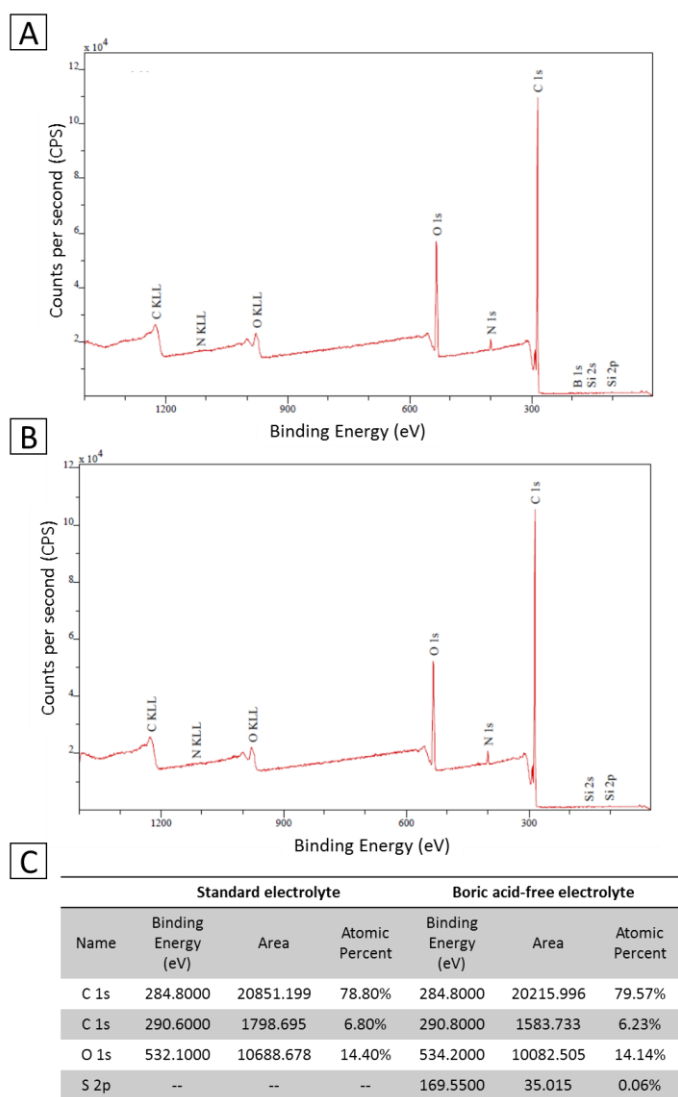


Figure 3.5 XPS spectra of a PC membrane following equilibration in (A) standard and (B) boric acid-free electrolyte, and corresponding (C) data table.

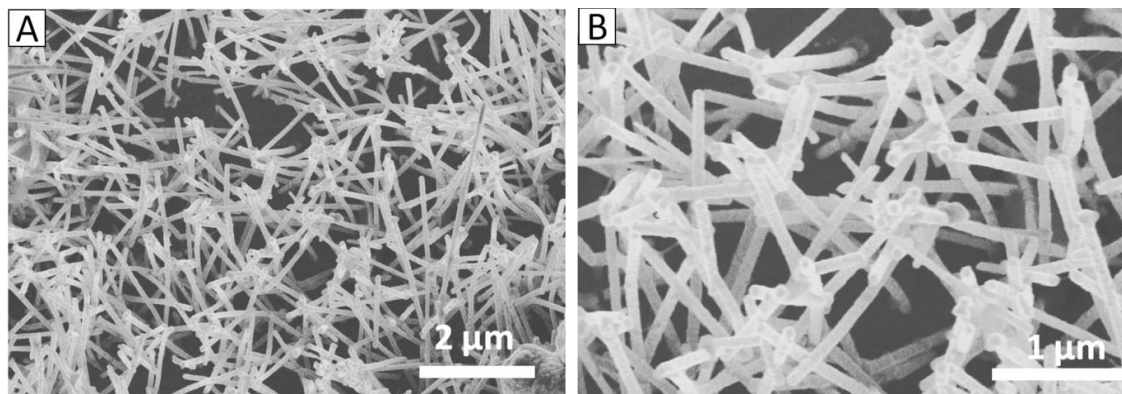


Figure 3.6 TEM images of nickel NWs synthesized within a PC membrane from the standard electrolyte.

The second method used to inhibit surface complexation involved the introduction of a competitive binder with enhanced affinity to boric acid, compared to Ni^{2+} , to the standard electrolyte. A 0.4 M aliquot of ethylene glycol was added to the electrolyte prior to ECD under standard conditions. The vicinal diol has been shown to successfully bind to boric acid and its derivatives in aqueous solutions.^{141, 169} Therefore, nickel ions must compete with the polyol for boric acid binding in the standard electrolyte.

Figure 3.7 shows that nickel NWs were formed as a result of the competition between nickel and ethylene glycol. Since ethylene glycol does not readily react with nickel ions, the NW formation was attributed to its interaction with boric acid. Reports from the literature demonstrate that the equilibrium constant for the formation of the ethylene glycol-borate complex is greater than that of the nickel-borate complex by approximately 10 orders of magnitude.^{132, 141} Therefore, borate preferentially interacted with ethylene glycol in the standard electrolyte. Figure 3.8 depicts the mechanism by which ethylene glycol impeded the accumulation of nickel along the pore wall. With the lack of disproportionation between the nickel concentration at the pore wall and central

pore region, nickel ECD once again occurred uniformly across the entire nanochannel to form NWs.

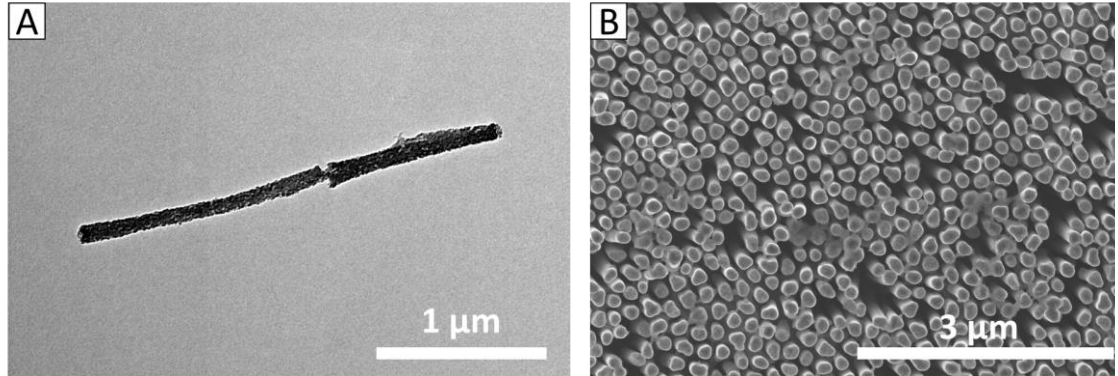


Figure 3.7 (A) TEM and (B) SEM image of nickel NWs synthesized from a solution containing 0.5 M NiSO₄, 0.4 M H₃BO₃, and 0.4 M ethylene glycol.

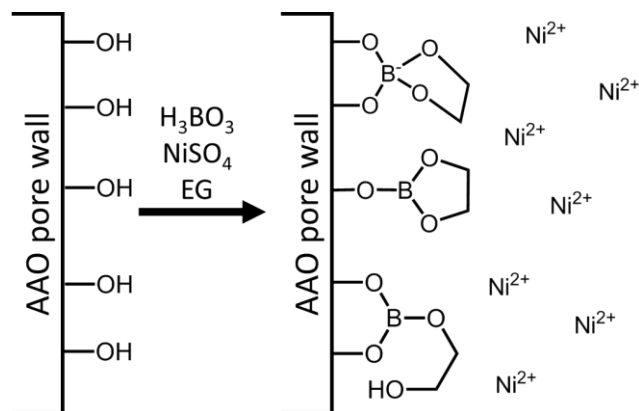


Figure 3.8 Schematic depiction of the adsorption of the ethylene glycol-borate complex to the AAO surface. Counter ions have been omitted for simplicity.

3.3.3. Effect of solvent rinsing on nanostructure morphology

The role of nickel-borate adsorption was further investigated by performing ECD in nickel-free electrolyte. Prior to ECD, the template was equilibrated in the standard nickel electrolyte for 10 minutes to allow sufficient time for the surface adsorption of the nickel-borate complex. The template was then washed with methanol to remove all unbound nickel ions. Deposition was performed in a 1 M NaSO₄ solution.

Figure 3.9 shows that very thin NTs were synthesized. Due to their fragile nature, the thin NTs were easily broken during TEM preparation, which made imaging intact NTs difficult. However, EDS analysis confirmed that the NT segments were in fact nickel. When the experiment was repeated with the BA-free electrolyte, no nickel nanostructures were observed. Since deposition was performed in a nickel-free solution after thoroughly washing the template, it can be concluded that the formation of NTs occurred through the reduction of surface adsorbed nickel ions. Following the methanol wash, the amount of adsorbed nickel in the absence of boric acid was not enough to facilitate continuous nickel deposition.

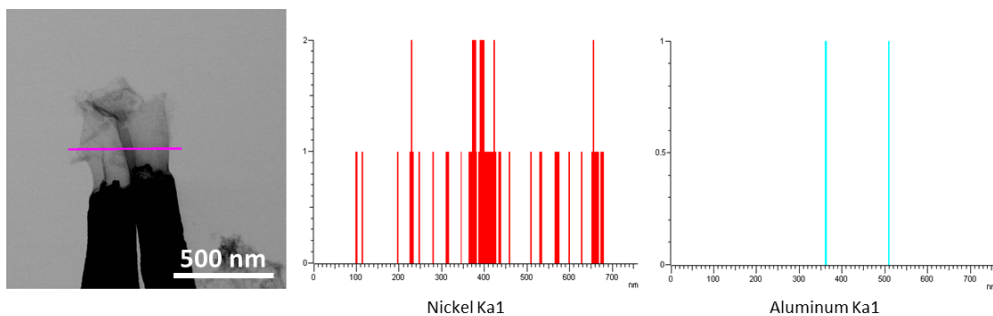


Figure 3.9 TEM image and corresponding EDS line scan of nickel NTs synthesized from 1 M NaSO₄ following equilibration in the standard electrolyte and a methanol wash.

Following the success of the solvent rinse experiment with the standard nickel plating solution, a series of equilibration-rinse-electrodeposition (E-R-D) steps were performed in sequence. The template was equilibrated in the standard Ni plating solution and rinsed with methanol as described above. Following ECD in NaSO₄, the template was reimmersed and sonicated in the Ni plating solution. Figure 3.10 shows TEM images of the resultant NTs obtained from 6, 9, 12, and 15 E-R-D cycles. Figure 3.11 clearly shows a linear correlation between the number of E-R-D cycles performed and the NT wall thickness.

The use of E-R-D cycles provides control over an additional NT dimension that had not been realized previously. Previous reports indicated that the wall thickness could be adjusted based on the sputtering time prior to ECD, however, strong correlative data was not evident.^{15, 170, 171} Conversely, the results above demonstrate that the nickel-borate surface-directed mechanism allows for controlled manipulation of the NT wall thickness. Exploiting this new parameter can lead to the synthesis of more robust and rigid nanostructures.

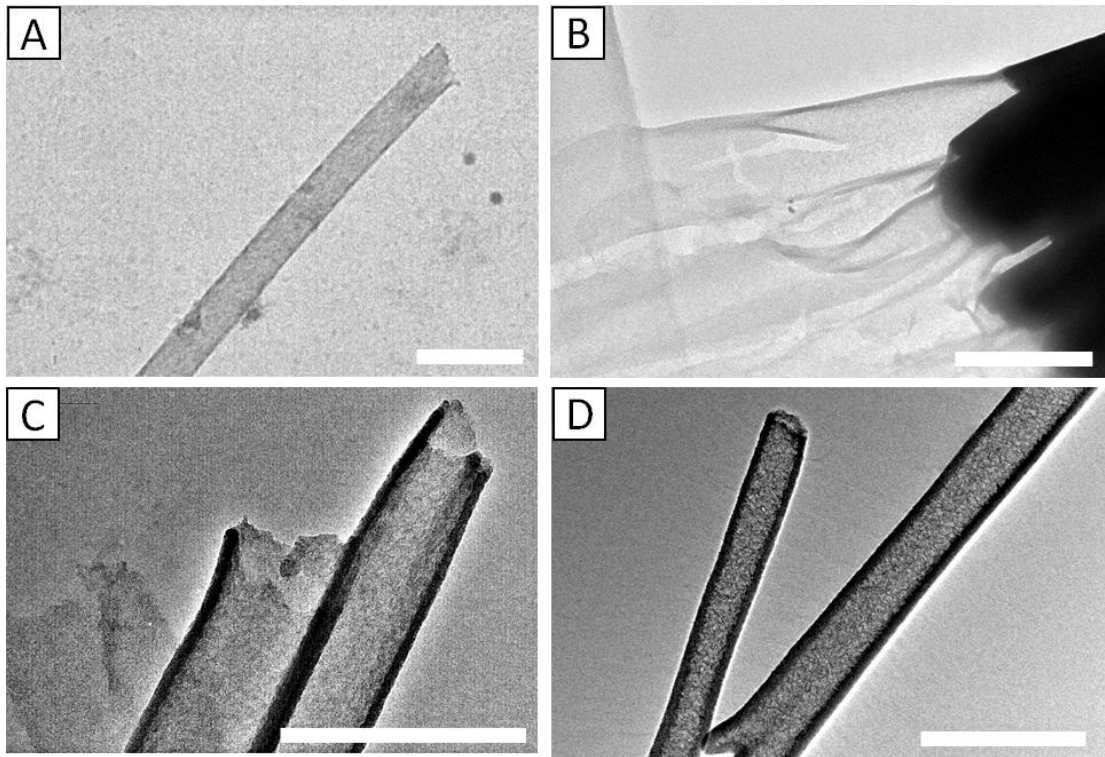


Figure 3.10 TEM images of nickel NTs synthesized from a series of (A) 6, (B) 9, (C) 12, (D) 15 equilibration-rinse-electrodeposition cycles.

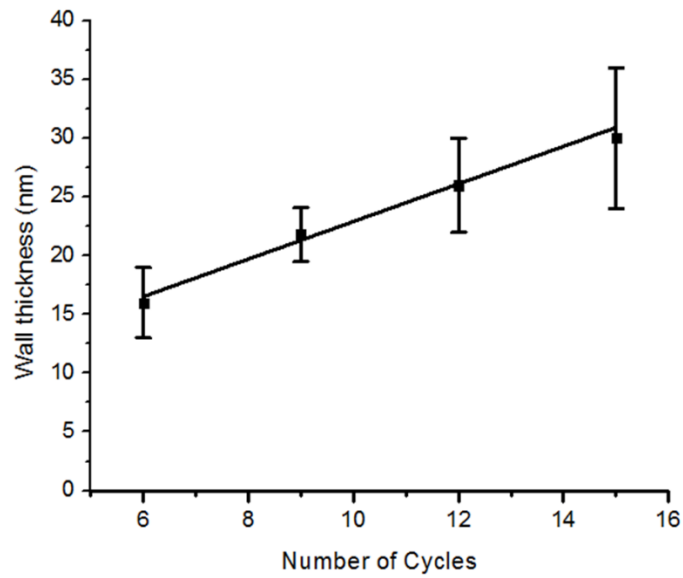


Figure 3.11 Plot depicting the change in NT wall thickness with successive series of equilibration-rinse-ECD cycles.

3.4. Conclusion

In this chapter we demonstrated the ability of the nickel-borate complex to adsorb to the AAO surface. The adsorbed complex plays a pivotal role in the determination of the morphology of electrochemically deposited nickel nanostructures. Adsorption of the complex to the alumina surface of the AAO template results in preferential deposition along the pore wall to form NTs. By inhibiting the adsorption of nickel-borate, through a competitive binder or lack of surface hydroxyl moieties, the growth of NWs is achieved. It was also demonstrated that the thickness of the NT walls can be controlled by removing non-adsorbed species from the template prior to deposition.

Chapter 4: Synthesis of advanced nanostructures via boric acid-controlled ECD

4.1. Introduction

With a clear understanding of the role of boric acid in nickel ECD, we are able to modify the morphology of various nanostructures simply by changing the electrolyte conditions. Additionally, the surface-directed electrochemical growth of metal deposits allows for well-controlled, conformal deposition onto intricate templates. As a result, the straightforward fabrication of complex nanostructures can be achieved. In this chapter we demonstrate the synthesis of nickel alloy, multisegmented, and three-dimensional (3D) nanostructures. In addition to demonstrating the ability of boric acid to direct the growth of nanoscale deposits, the experiments presented in this chapter were used as a proof-of-concept for the facile synthesis of intricate nanostructures for application in magnetic data storage, nanoelectronics, and energy storage.

4.2. Experimental method

4.2.1. Codeposition of nickel alloys

The electrodeposition of nickel alloys was carried out using the procedure described in Section 2.2.1. Briefly, flat-top gold NWs were deposited into the pores of the exposed AAO in the working electrode. Nickel alloys were synthesized by codeposition from electrolyte solutions containing iron and/or cobalt, according to Table 4.1. A potential of -1 V was applied for 30 min in all deposition experiments.

The resultant nanostructures were characterized by TEM and SEM as described in Section 2.2.2. In addition to imaging, energy-dispersive X-ray spectroscopy (EDS) was

performed using an Oxford (INCA 250) system to analyze the elemental composition of the alloys. During EDS, an accelerating voltage of 10 kV was used.

Table 4.1 Electrolyte composition for the synthesis of nickel alloy nanostructures. All solutions were prepared in deionized water.

Alloy Description	NiSO₄	CoSO₄	FeSO₄	H₃BO₃	NaSO₄
NiFe standard	0.25 M	--	0.25 M	0.4 M	--
NiFe BA-free	0.25 M	--	0.25 M		0.06 M
NiCo standard	0.25 M	0.25 M	--	0.4 M	--
NiCo BA-free	0.25 M	0.25 M	--	--	0.06 M
NiFeCo standard	0.16 M	0.16 M	0.16 M	0.4 M	--
NiFeCo BA-free	0.16 M	0.16 M	0.16 M	--	0.06 M

4.2.2. Synthesis of segmented nickel nanostructures

Following the electrodeposition of gold NWs, sequential deposition cycles were performed in the standard and BA-free electrolyte to generate NT and NW segments, respectively. Prior to each cycle, the working electrode was sonicated in the appropriate electrolyte for 10 min to ensure diffusion of the new electrolyte into the template pores. After each cycle, the electrodes were washed and sonicated in deionized water before being placed in the next solution. For the first 7 cycles, ECD with the standard electrolyte was performed at -1 V for 2 minutes, whereas ECD with the BA-free electrolyte was performed at -1 V for 45 seconds. The deposition times were shortened for the last 4 cycles in order to observe its effect on segment length. The potential was applied for 1 minute with the standard electrolyte and 20 seconds with the BA-free electrolyte. Characterization with TEM analysis was performed as described in Section 2.2.2.

4.2.3. Synthesis of 3D nanostructures

A 3D interconnected porous AAO membrane with regular branched regions was prepared in-house with a two-step anodization process, as previously reported.¹⁷² Briefly, pure aluminum foil was degreased in acetone and electropolished in a 1:5 perchloric acid: ethanol solution at 15 V, 3 °C for 5 min. Both anodization steps were performed in a 0.3 M oxalic acid solution maintained at 8 °C. During the first anodization, a constant potential of 40 V was applied for 7 hours. The resulting porous alumina film was etched in a mixture of phosphoric acid (6 wt%) and chromic acid (1.5 wt%) at 60 °C for 4 hrs and 40 min. Voltage stepping was used during the second anodization to generate interconnected, branched pores. Figure 4.1 shows the voltage profile for the synthesis of one branched region. The voltage was stepped from 40 V to 20 V in 2 V increments with each step lasting 30 s each. The voltage was ramped down to 15 V at the end of the second anodization to thin the barrier layer.

The pore diameter was enlarged to ca. 80 nm with a pore widening step. To achieve this, the AAO was placed in a 5% H₃PO₄ at 38°C for 11.5 minutes. The template was then immersed in a solution containing 0.4 M copper chloride and 5% HCl until the porous AAO film separated from the aluminum foil. Gold was sputtered on the branched side of the resultant AAO membrane to ensure for good electrical contact during ECD. The deposition was performed as described in Section 2.2.1.

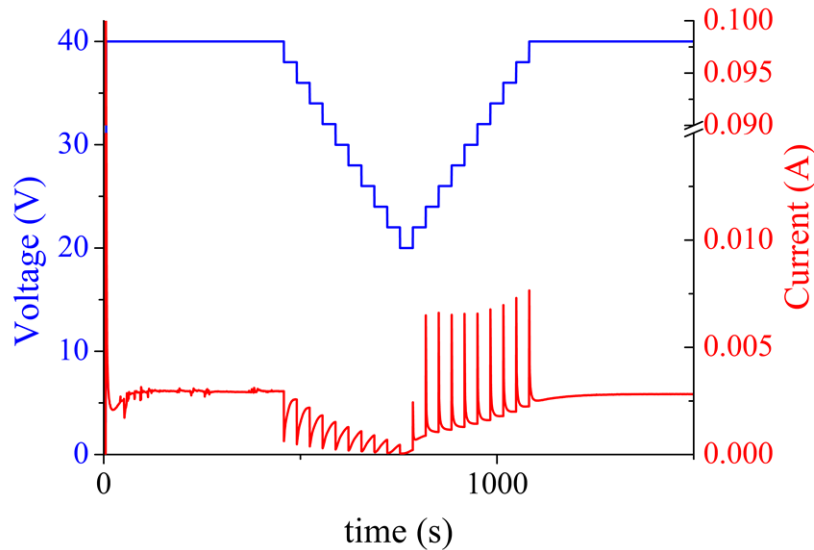


Figure 4.1 Voltage profile of a voltage step for the synthesis of branched pores within an AAO membrane.

4.3. Results and discussion

4.3.1. Nickel alloy nanotubes

The ability of nickel to alloy with most metals has been exploited in a variety of industries, including the manufacturing of aircraft turbines, medical instruments, and nuclear power turbines. Nanostructures of nickel alloys hold great promise for applications in ultra-high density magnetic data storage.^{48, 173-179} The use of periodic arrays of magnetic nanostructures has been shown to provide 2.5 times the storage density compared to conventional magnetic thin film media.¹⁸⁰ As a result, a shift towards the investigation of the magnetic properties of 1D alloy structures has recently occurred.^{15, 28, 56, 94, 100, 181, 182} Typically, alloy nanostructures composed of nickel, cobalt, and iron are studied for magnetic applications, due to the success of these alloy compositions in thin film studies.^{174, 175, 180} In this section, we present alloy NTs and

NWs that were synthesized based on the boric acid-controlled surface-directed mechanism described in Chapter 3.

Figure 4.2 shows TEM images with corresponding EDS line scans of the NiFe, NiCo, and NiFeCo nanostructures synthesized with boric acid. As predicted by the boric acid-controlled surface-directed growth mechanism, NTs were formed from all three standard electrolytes. The hollow NT void is clearly visible in the TEM images. Additional support for the NT structure was obtained from EDS line scans performed perpendicular to the NT axis. The shape of each of the elemental line scans is characteristic of the NT structure. A low signal intensity was obtained throughout the central region of the structure due to the hollow void. Conversely, the outer edges exhibited the highest signal intensity due to the thickness of the NT wall. Based on a comparison of the overall signal intensities for each metal, elemental analysis revealed that the NTs comprise approximately equivalent concentrations of each metal. This result corresponds with the elemental composition expected for ECD from an equimolar alloy plating solution.

Figure 4.3 shows SEM images of the alloy nanostructures prepared from standard electrolytes. As described before, the large aspect ratio and thin walls of the NTs that form in the presence of boric acid cause the structures to collapse onto one another to form a NT film over the gold base electrodes. The NT film can be seen in all three alloy samples synthesized from standard electrolytes.

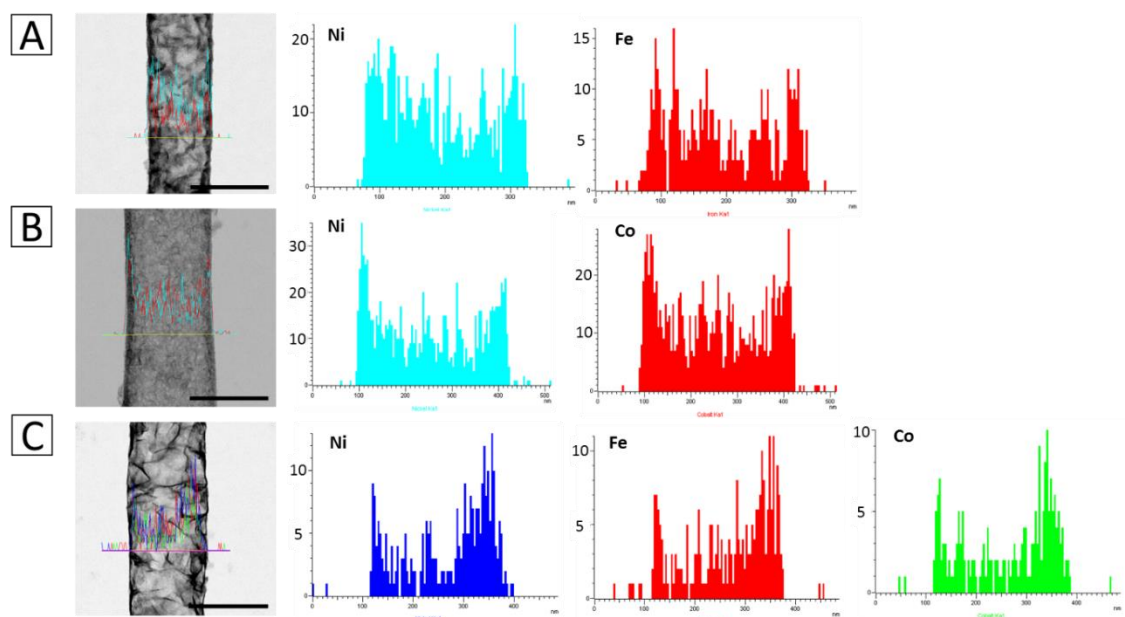


Figure 4.2 TEM images with corresponding EDS line scans of nickel alloy NTs synthesized from (A) NiFe standard, (B) NiCo standard, and (C) NiFeCo standard electrolytes. Scale bar represents 300 nm.

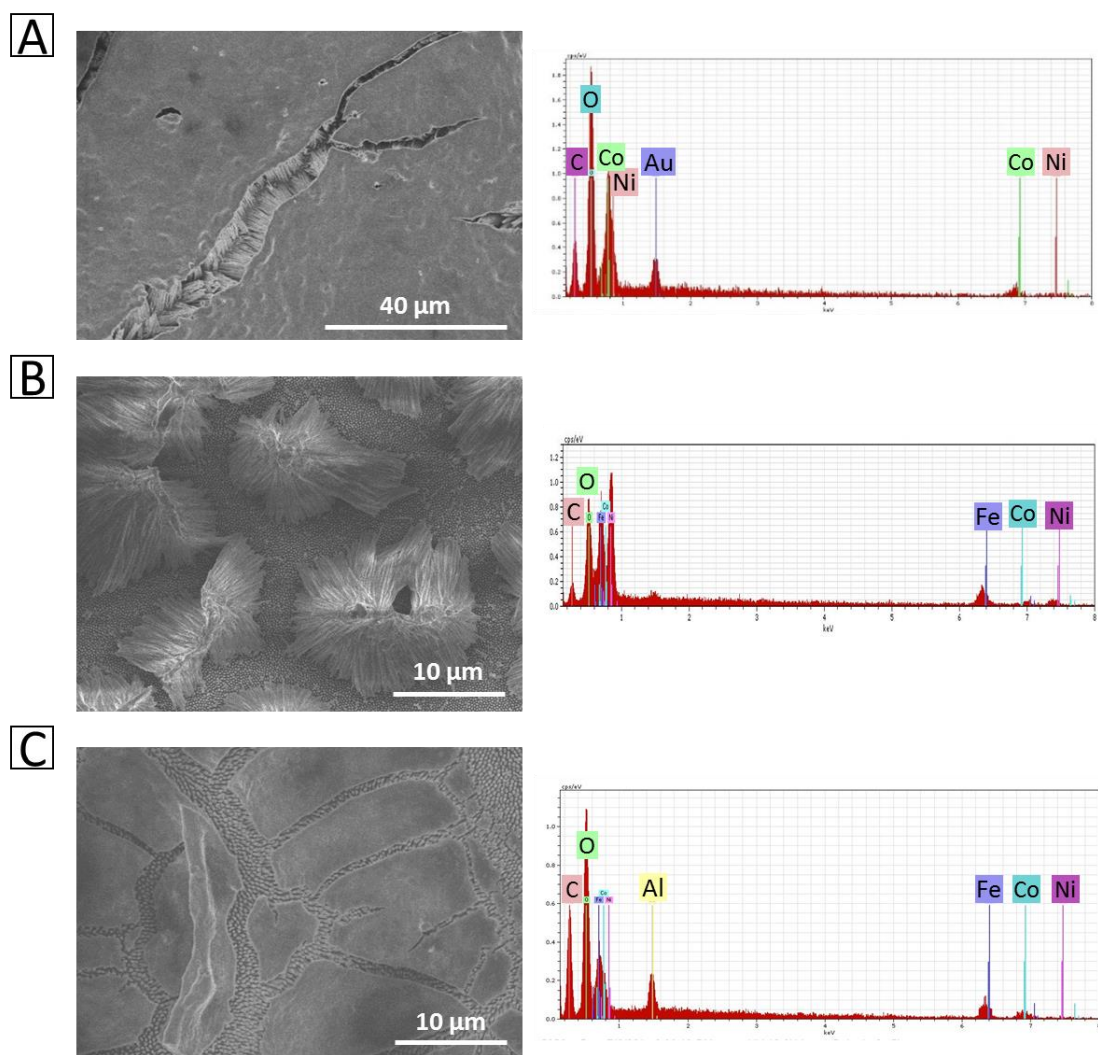


Figure 4.3 SEM images and corresponding EDS spectra of nickel alloys synthesized from solution (A) NiCo standard, (B) NiFe standard, and (C) NiFeCo standard electrolytes.

In comparison, the alloy nanostructures synthesized from BA-free solutions were capable of remaining upright following the removal of the AAO template, as seen in Figure 4.4. Despite the appearance of NT tips, the TEM images in Figure 4.5 reveal that the rigidity of the nanostructures originates from the fully-filled NW morphology. These results are consistent with the nickel NT structures formed from the BA-free electrolyte in Chapter 2.

In addition to the TEM images, analysis of the EDS line scans provides further support for the NW morphology. Unlike NTs, the thickest point of the NW structure is the core. Therefore, a high signal intensity at the center of the nanostructure is indicative of NW morphology. With the exception of the NiFe NW, the signal intensities revealed that the NWs comprise approximately equivalent concentrations of each metal, which again was expected from the equimolar alloy plating solutions. The disproportionate ratio of Ni: Fe can be attributed to the varying influence of the deposition conditions on each metal. Factors such as overpotential and additives may affect the deposition of nickel and iron to different degrees, leading to a higher deposition of iron. The disproportionate concentration is likely more apparent in the fully-filled NWs due to the greater volume of analyzed material.

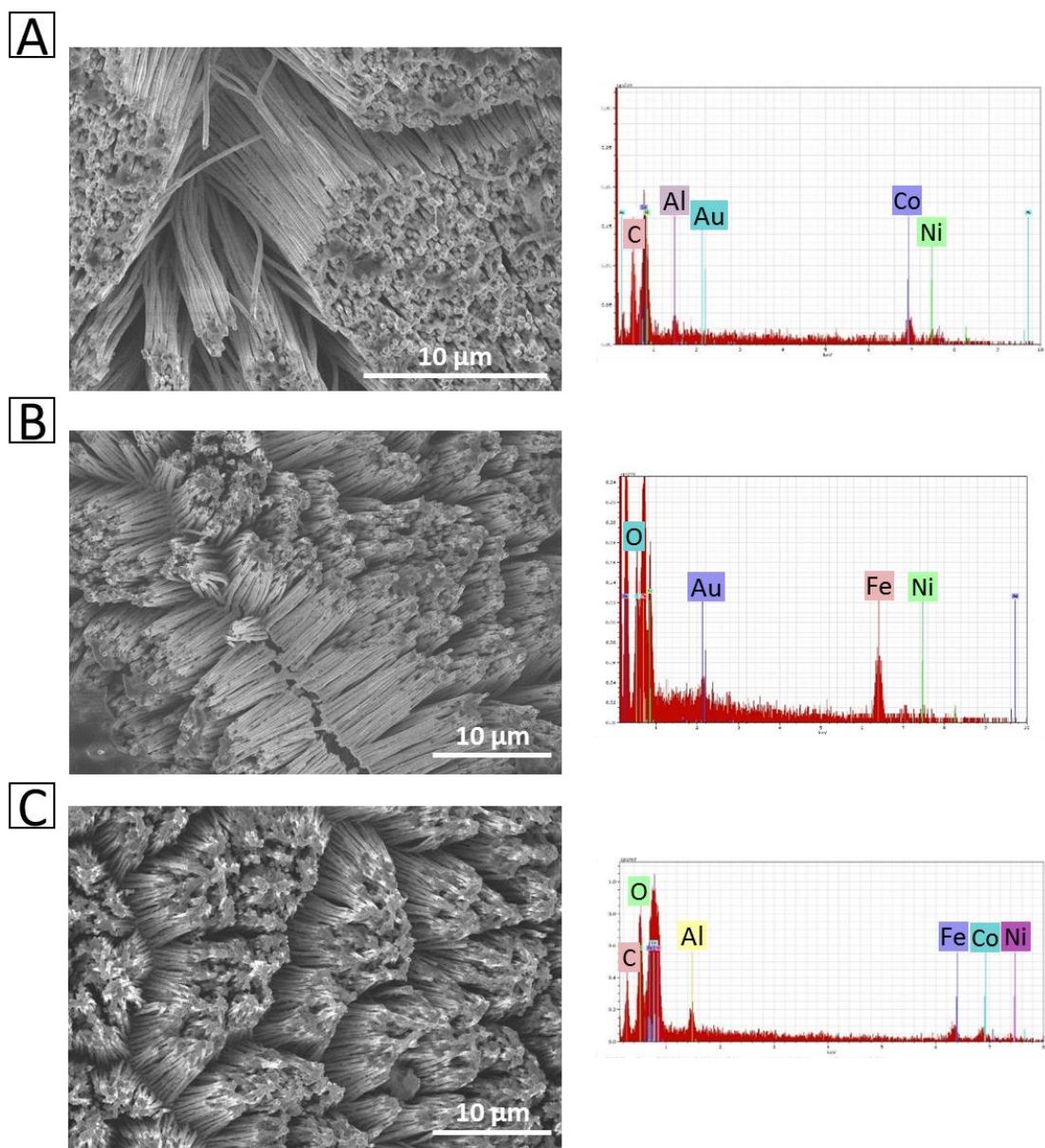


Figure 4.4 SEM images and corresponding EDS spectra of nickel alloys synthesized from (A) NiCo BA-free, (B) NiFe BA-free, and (C) NiFeCo BA-free electrolytes.

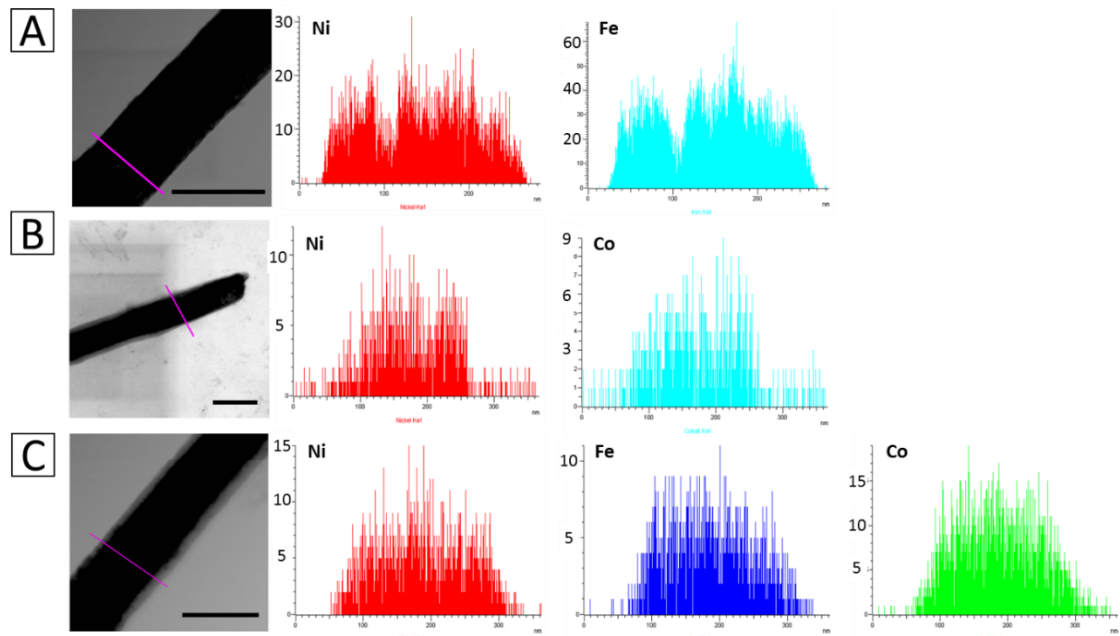


Figure 4.5 TEM images with corresponding EDS line scans of nickel alloy NWs synthesized from (A) NiFe BA-free, (B) NiCo BA-free, (C) NiFeCo BA-free electrolytes. Scale bar represents 300 nm.

These results reveal that the role of boric acid on the growth mechanism of nickel is maintained during ECD from a mixture of metal ions, providing a facile approach to the synthesis of nickel alloy NTs and NWs. Furthermore, it can be suggested that boric acid is capable of directing the 1D electrochemical growth of other transition metals, including iron and cobalt, through the formation of a surface complex. However, a more detailed investigation is required in order to confirm the borate effect is maintained during ECD of such metals. The resultant alloy nanostructures presented in this section can be further studied for use as magnetic data storage media.

4.3.2. Segmented nickel nanostructures

Recently, considerable attention has been focused on 1D heterostructures due to their unique properties and their potential application in nanoelectronic devices, and resistive random access memory. To date, the majority of longitudinally segmented

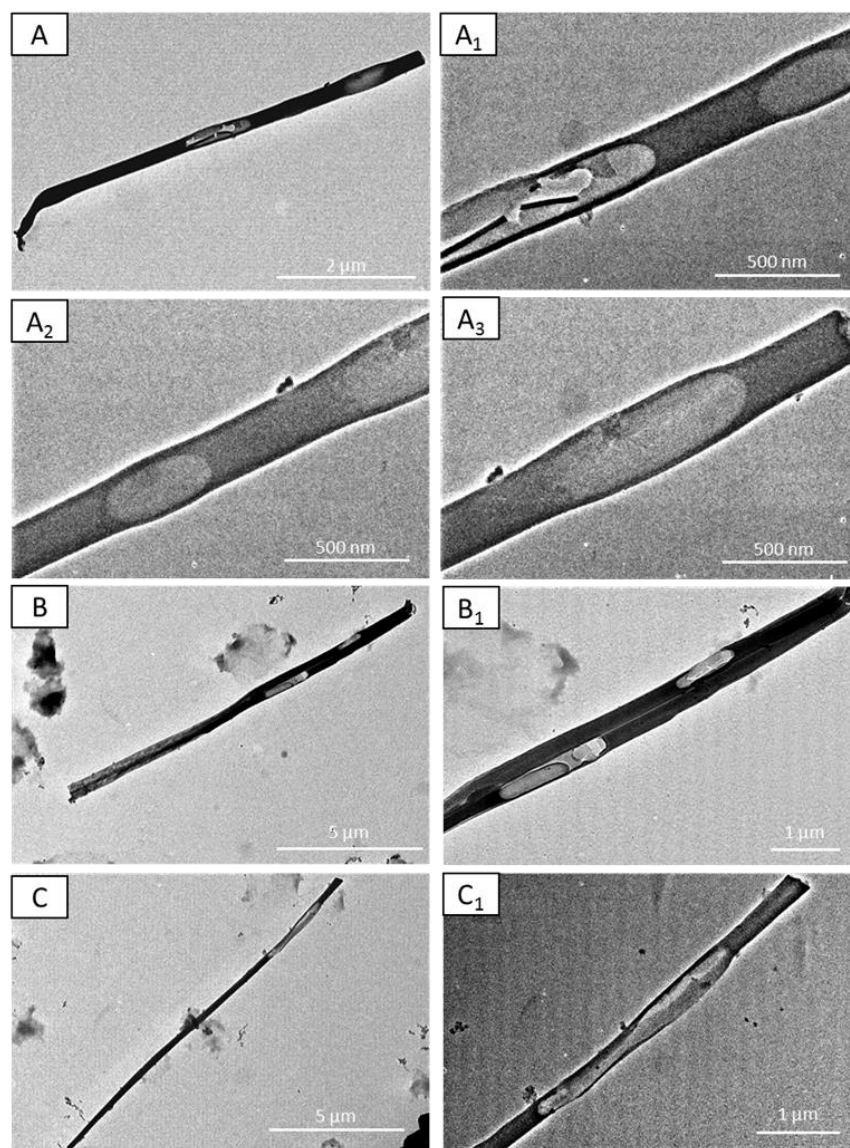
heterostructures found in the literature are composed of NW segments of various semiconducting materials.¹⁸³⁻¹⁹⁰ Several reports cite the synthesis of NT segments composed of carbon or silicon.^{191, 192} However, there have been few demonstrations of heterostructures containing metal NT segments.¹⁹³ Additionally, the synthesis methods employed often limit the number of NT-NW segments that can be incorporated into the structure. The majority of the research has focused on nanostructures containing a maximum of 2 NT segments. Since the material and structure greatly affect the properties of the resultant structure, it is important to synthesize as many permutations as possible.

In order to remedy the current deficiency, we exploit the role of boric acid in the ECD of nickel to synthesize multisegmented 1D nanostructures composed of nickel NT and NW segments. The various NT and NW segments were generated by successive electrodeposition cycles in the standard and BA-free electrolyte, respectively. Figure 4.6 shows that segmented 1D nanostructures composed of well-defined NT and NW sections were formed. Due to the encapsulation of electrolyte during synthesis, some of the NT sections ruptured under the high vacuum of the TEM. As mentioned in Section 4.2.2, two different deposition schemes were employed during the synthesis of the segmented nanostructures.

The length of each NT segment is provided in Figure 4.6 D. From this data, there does not appear to be a definitive demarcation between segments originating from the long and short deposition cycles. However, it can be stated with considerable confidence that the 1718 nm and 3010 nm segments were synthesized from a 2 min deposition cycle, whereas the segments between 420 nm and 973 nm likely originated from a 1 min

deposition cycle. The wide variation in segment size can be attributed to the incomplete rinsing of the nanochannel prior to equilibration in the new electrolyte.

Initially, fresh electrolyte must travel tens of microns to reach the deposition interface. Despite the sonication step, the previous electrolyte may not have been fully rinsed out of the nanochannel prior to sonication and equilibration in the new electrolyte. Therefore, applying the potential resulted in continued deposition and growth of the same NT or NW segment. In the case of the NT segment, it is possible that the nickel-borate complex remained attached to the pore wall even after the electrolyte had been washed away, which would result in enhanced deposition along the wall before the formation of the NW segment. Further optimization of the rinse and equilibration steps is required in order to achieve precise control over the synthesis of uniform NT and NW segments.



NT segment	Length (nm)
A ₁	973
A ₂	420
A ₃	833
B ₁	970
B ₁	1718
C ₁	3010

Figure 4.6 TEM images of (A-C) nickel segmented nanostructures synthesized from successive deposition cycles in the standard and BA-free electrolyte. Subsets represent high magnification images of individual segments. (D) Table of NT segment lengths corresponding to A-C.

4.3.3. Three-dimensional nanostructure network

Finally we employed the surface-directed growth of nickel to the preparation of 3D nanostructures as a model for the fabrication of multidimensional electrical energy storage devices. The study of nanostructures for energy storage has matured to such a point that a drastic change is required to further advance the technology. Three-dimensional nanoelectrodes offer a means to increase energy storage without hindering power storage, and propel energy storage devices beyond the current limits.^{194, 195} Common approaches to the synthesis of 3D electrodes include atomic layer deposition and ECD with modified AAO templates. In order to generate a 3D AAO template, the aluminum anodization process is altered to generate interconnecting channels at designated positions along the pore axis. A critical aspect of 3D nanostructure fabrication is the conformal deposition of material throughout the horizontal and vertical nanochannels.

ECD provides an ideal method of synthesis for these structures since the electrolyte is capable of reaching into the deep recesses of complex nanotemplates prior to the onset of the overpotential. However, traditional deposition methods generate growth primarily in the direction of current flow, i.e. perpendicular to the electrode surface. Fast deposition along the vertical nanochannels can impede sufficient deposition within the horizontal nanochannels, as was observed with the ECD of nickel from the BA-free electrolyte in Chapter 2. As a result, complete deposition into the horizontal nanochannels may be impeded which would prevent the formation of a fully interconnected 3D electrode. In contrast, the surface-directed growth mechanism

presented in Chapter 3 provides a synthesis method that ensures uniform growth throughout the entire template geometry.

SEM images in Figure 4.7 show the nickel nanostructures synthesized from the 3D interconnected AAO membrane in the standard electrolyte. The first branched region was observed 4 μm from the base of the membrane. The high magnification images reveal the Y-shaped branched structure, with the main, parallel structure appearing more rigid than the branched structure. Although it is difficult to discern with SEM, the branched structure resembles the collapsed NT film obtained from the commercial AAO. After the first 6 μm the typical NT film is observed for the entire 3D network.

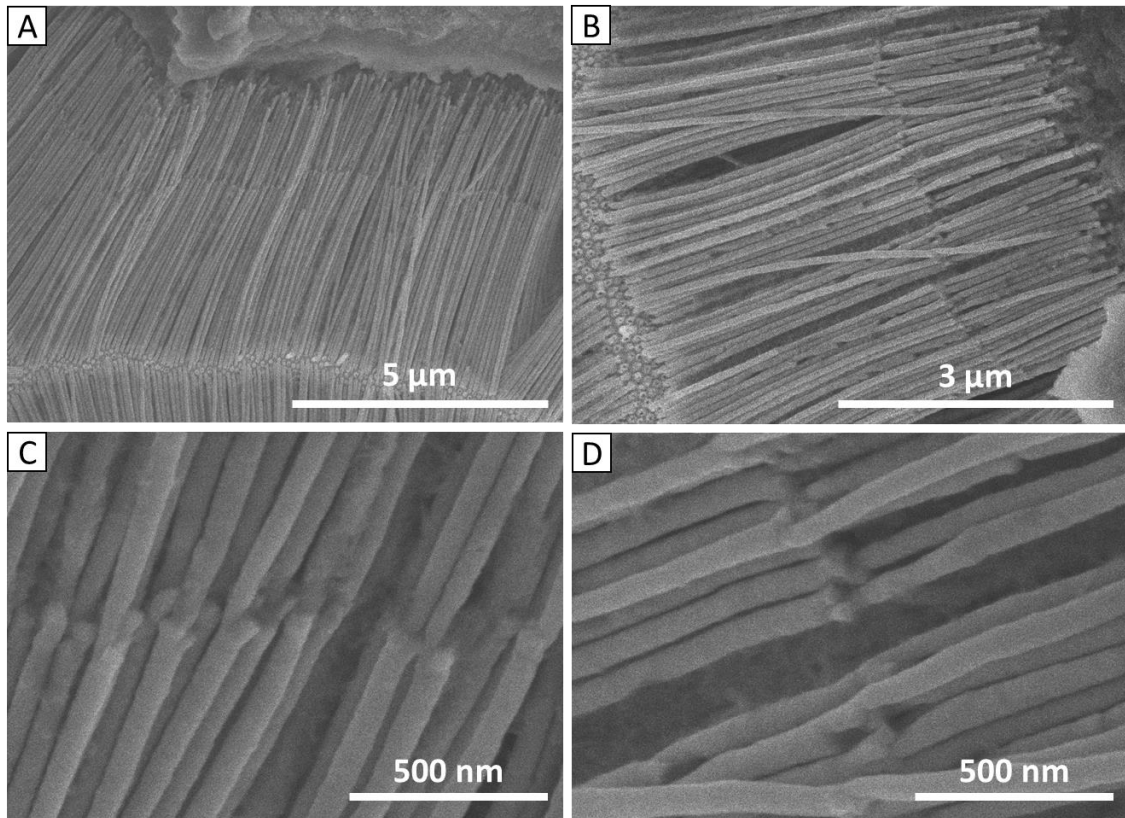


Figure 4.7 SEM images of a 3D nickel nanostructure network synthesized within a homemade 3D AAO template in the standard electrolyte.

The interconnected network allowed neighboring NTs to remain intact following the removal of the AAO template, which complicated TEM imaging of the structures. Figure 4.8 A shows a typical aggregation of nanostructures that was observed due to the interconnected branched structures. The drastic decrease in pore diameter compared to the commercial AAO resulted in the deposition of NWs. However, as Figure 4.8 B demonstrates, NTs were also present in the sample. Optimization of the deposition conditions must be performed in order to ensure uniform NT growth. Despite the presence of nickel NWs, there appears to be NT growth at the branched regions, which corresponds well with the SEM images.

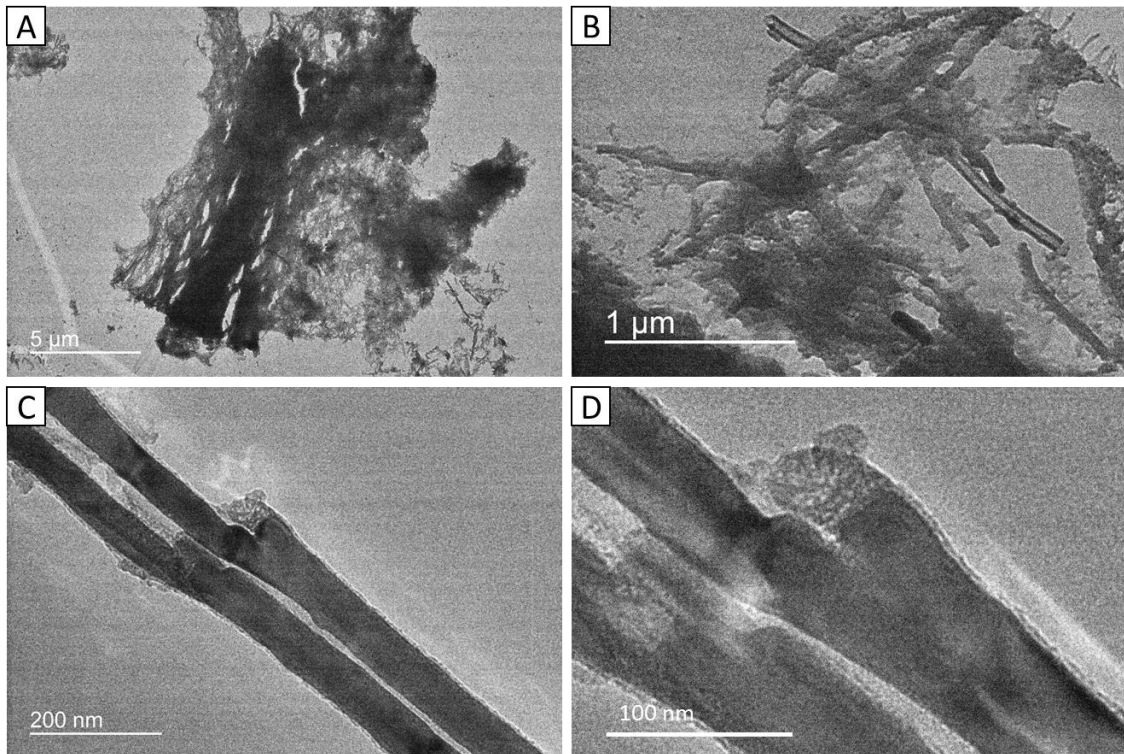


Figure 4.8 TEM images of nickel nanostructures synthesized from the standard electrolyte with the 3D interconnected AAO template.

4.4. Conclusion

In this chapter we demonstrate the practical applications for the boric acid-controlled surface-directed ECD growth of metal nanostructures, beyond the generation of simple NTs and NWs. Boric acid was shown to direct the ECD of alloy nanostructures comprised of nickel, iron, and cobalt. As a result, the NTs and NWs with nearly identical chemical composition can be compared to determine the influence of morphology on the magnetic properties. In addition, the surface-directed growth mechanism was employed to generate segmented nickel nanostructures. The formation of the heterostructures by simple electrolyte exchange not only offers further proof for the role of boric acid, but provides a novel route to synthesizing multisegmented nanostructures for application in nanoelectronic devices. Finally, the surface-directed growth of nickel was applied to the synthesis of a 3D nanostructure network. Despite the presence of NTs and NWs in the sample, the microscopy images indicate that the deposition followed the complex template geometry to form an interconnected network.

Chapter 5: Summary and Future Work

5.1. Summary

The overall goal of this research was to investigate the factors controlling the ECD of NT versus NW structures in the absence of physical modifiers, such as annular electrodes and template modification. We demonstrated that boric acid concentration was a determining factor in the morphology of the 1D nanostructures. In doing so, we have highlighted the importance of fully investigating the effects of additives in electrochemical plating solutions, specifically for the deposition of nanostructures. The conventional view of boric acid in electroplating solution is that of a buffer. Yet we have clearly confirmed it plays a significant role in the determination of 1D nanostructure morphology.

In Chapter 2, electrochemical analysis of nickel deposition revealed that the presence of boric acid in the electrolyte drastically modified the deposition mechanism. The fundamental requirement for nickel NT growth, in the absence of physical modifiers, was proven to be the surface adsorption of the nickel-borate complex to the template surface. Inhibition of the complex adsorption, by removing the surface hydroxyl groups or adding a competitive binder to the electrolyte, resulted in NW formation. Additionally, the adsorption of the nickel-borate complex allowed for enhanced control of the NT wall thickness with multiple E-R-D cycles.

Finally the surface-directed ECD of nickel was employed to synthesize a variety of advanced nanostructures. The role of boric acid was shown to control the ECD of nickel alloys, indicating that this growth mechanism can be applied to additional metals.

Multisegmented nanostructures were synthesized by simply alternating the electrolyte solution between the standard and BA-free solutions. Additionally, the surface-directed growth allowed for continued deposition on the horizontally and vertically-aligned pores of a modified AAO template, which generated a 3D interconnected nanostructure.

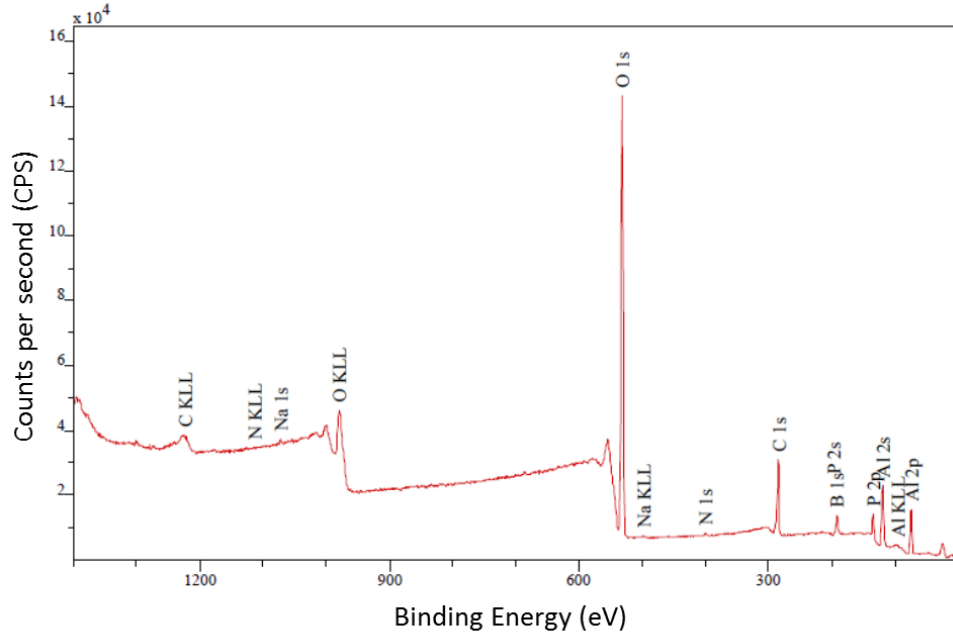
5.2. Future Work

Throughout this work, we have thoroughly demonstrated the effect of boric acid on the morphology of 1D nickel nanostructures. Continued work in this area will involve the study of this growth mechanism in the ECD of additional metal nanostructures. For instance, the alloy NT and NW synthesis indicates that iron and cobalt 1D morphology may also be controlled by boric acid. The experiments performed in this work would need to be applied to the deposition of these metals in order to confirm the boric acid effect is maintained.

Additionally, the advanced structures require further optimization before they can be investigated for their respective applications. Optimization of the multisegmented nanostructure requires improvements in the rinse step of the deposition process. In order to obtain uniformity in the segment lengths, the old electrolyte must be fully removed and replaced by new electrolyte before the potential is applied. Furthermore, the charge transferred can be monitored to determine the deposition duration and to provide more control over the length of each segment. Optimization of the 3D nanostructure network involves modifying the deposition conditions to suit the diminished pore size. The synthesis of NWs from the standard electrolyte indicates that the deposition must be shortened. It is likely that NTs initially form, but become fully-filled NWs as the deposition continues for an extended period of time.

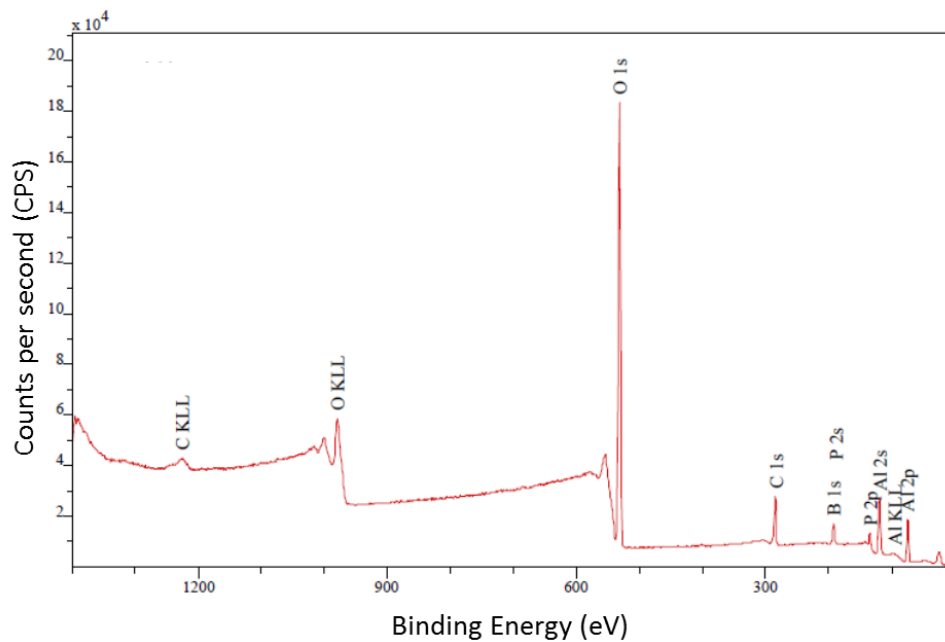
Appendix

Figure A.1 XPS spectra and corresponding data table for an AAO membrane following equilibration in deionized water.



Name	Binding Energy (eV)	Area	Atomic Percent
C 1s	284.8000	5634.741	25.46%
O 1s	532.0000	32451.090	52.27%
Al 2p	74.9000	3420.521	22.27%

Figure A.2 XPS spectra and corresponding data table for an AAO membrane following equilibration in 0.4 M boric acid.



Name	Binding Energy (eV)	Area	Atomic Percent
C 1s	284.8000	4704.233	18.48%
O 1s	532.1000	42135.543	59.00%
A; 2p	74.6000	3979.590	22.52%

Bibliography

1. Voelcker, J., Winchester disks reach for a gigabyte. *Ieee Spectrum* **1987**, 24, (2), 64-67.
2. ST506 Preliminary OEM Manual. **1981**, 1-39.
3. Yan, C.; Le, B. H.; Kang, D. J., Ultrasensitive single crystalline TeO₂ nanowire based hydrogen gas sensors. *Journal of Materials Chemistry A* **2014**, 2, (15), 5394-5398.
4. Feng, C. X.; Xu, G. Q.; Liu, H. P.; Lv, J.; Zheng, Z. X.; Wu, Y. C., A Flow-Injection Photoelectrochemical Sensor Based on TiO₂ Nanotube Arrays for Organic Compound Detection. *Journal of the Electrochemical Society* **2014**, 161, (3), H57-H61.
5. Wang, Y.; Chen, J.; Zhou, C. P.; Zhou, L.; Kong, Y. Y.; Long, H. Y.; Zhong, S. A., A novel self-cleaning, non-enzymatic glucose sensor working under a very low applied potential based on a Pt nanoparticle-decorated TiO₂ nanotube array electrode. *Electrochimica Acta* **2014**, 115, 269-276.
6. Pallarola, D.; Schneckeburger, M.; Spatz, J. P.; Pacholski, C., Real-time monitoring of electrochemical controlled protein adsorption by a plasmonic nanowire based sensor. *Chemical Communications* **2013**, 49, (75), 8326-8328.
7. Ma, Z.; Liu, Q.; Cui, Z. M.; Bian, S. W.; Song, W. G., Parallel array of Pt/polyoxometalates composite nanotubes with stepwise inside diameter control and its application in catalysis. *Journal of Physical Chemistry C* **2008**, 112, (24), 8875-8880.
8. Du, C. Y.; Chen, M.; Wang, W. G.; Tan, Q.; Xiong, K.; Yin, G. P., Platinum-based intermetallic nanotubes with a core-shell structure as highly active and durable catalysts for fuel cell applications. *Journal of Power Sources* **2013**, 240, 630-635.

9. Xu, Y.; Lee, H.; Hu, Y.; Huang, J.; Kim, S.; Yun, M., Detection and Identification of Breast Cancer Volatile Organic Compounds Biomarkers Using Highly-Sensitive Single Nanowire Array on a Chip. *Journal of Biomedical Nanotechnology* **2013**, 9, (7), 1164-1172.
10. Hu, Q.; Liu, Y. Q.; Li, N.; Cheng, C.; Xu, S. G.; Wang, N.; Qin, W.; Tang, B. Z., Ni-NTA-coated nanowire materials for protein enrichment and the application in a medical device used for blood glucose degradation *Nano* **2013**, 8, (3).
11. Stoermer, R. L.; Cederquist, K. B.; McFarland, S. K.; Sha, M. Y.; Penn, S. G.; Keating, C. D., Coupling molecular beacons to barcoded metal nanowires for multiplexed, sealed chamber DNA bioassays. *Journal of the American Chemical Society* **2006**, 128, (51), 16892-16903.
12. Ding, L.-X.; Li, G.-R.; Wang, Z.-L.; Liu, Z.-Q.; Liu, H.; Tong, Y.-X., Porous Ni@Pt Core-Shell Nanotube Array Electrocatalyst with High Activity and Stability for Methanol Oxidation. *Chemistry-a European Journal* **2012**, 18, (27), 8386-8391.
13. Yan, Z. Y.; Li, B.; Yang, D. J.; Ma, J. X., Pt nanowire electrocatalysts for proton exchange membrane fuel cells. *Chinese Journal of Catalysis* **2013**, 34, (8), 1471-1481.
14. Narayanan, T. N.; Shaijumon, M. M.; Ajayan, P. M.; Anantharaman, M. R., Synthesis of high coercivity cobalt nanotubes with acetate precursors and elucidation of the mechanism of growth. *Journal of Physical Chemistry C* **2008**, 112, (37), 14281-14285.
15. Han, X. F.; Shamaila, S.; Sharif, R.; Chen, J. Y.; Liu, H. R.; Liu, D. P., Structural and Magnetic Properties of Various Ferromagnetic Nanotubes. *Advanced Materials* **2009**, 21, (45), 4619-4624.

16. Paunovic, M.; Schlesinger, M., *Fundamentals of electrochemical deposition*. 2nd ed.; Wiley: Hoboken, 2006.
17. Shi, S.; Wang, X.; Xu, C.; Yuan, J.; Fang, J.; Liu, S., Simulation and fabrication of two Cu TSV electroplating methods for wafer-level 3D integrated circuits packaging. *Sensors and Actuators a-Physical* **2013**, 203, 52-61.
18. Riemer, S. C.; Tabakovic, I.; Gong, J.; Lam, H. T.; Kief, M. T.; Ostrowski, M. H.; Qiu, J. Method and system for magnetic recording media. 2009.
19. Kanani, N., *Electroplating: Basic principles, processes and practice*. Elsevier: New York, 2004.
20. Burk, J. J.; Buratto, S. K., Electrodeposition of Pt Nanoparticle Catalysts from H₂Pt(OH)₆ and Their Application in PEM Fuel Cells. *Journal of Physical Chemistry C* **2013**, 117, (37), 18957-18966.
21. Bian, J.-C.; Li, Z.; Chen, Z.-D.; He, H.-Y.; Zhang, X.-W.; Li, X.; Han, G.-R., Electrodeposition of silver nanoparticle arrays on ITO coated glass and their application as reproducible surface-enhanced Raman scattering substrate. *Applied Surface Science* **2011**, 258, (5), 1831-1835.
22. Li, W. J.; Yu, W. L.; Yen, C. Y., Pulsed electrodeposition of Bi₂Te₃ and Bi₂Te₃/Te nanowire arrays from a DMSO solution. *Electrochimica Acta* **2011**, 58, 510-515.
23. Hernandez-Pagan, E. A.; Wang, W.; Mallouk, T. E., Template Electrodeposition of Single-Phase p- and n-Type Copper Indium Diselenide (CuInSe₂) Nanowire Arrays. *Acs Nano* **2011**, 5, (4), 3237-3241.

24. Li, Y.; Luo, S. L.; Wei, Z. D.; Meng, D. H.; Ding, M. Y.; Liu, C. B., Electrodeposition technique-dependent photoelectrochemical and photocatalytic properties of an In₂S₃/TiO₂ nanotube array. *Physical Chemistry Chemical Physics* **2014**, 16, (9), 4361-4368.
25. Brumlik, C. J.; Martin, C. R., Template synthesis of metal microtubules. *Journal of the American Chemical Society* **1991**, 113, (8), 3174-3175.
26. Chen, J. Y.; Shi, D. W.; Ahmad, N.; Liu, D. P.; Zhou, W. P.; Han, X. F., Fabrication and magnetic properties of La-X (X = Co, Ni, and Fe) nanotube arrays prepared by electrodeposition methods. *Journal of Applied Physics* **2013**, 114, (5), 054303.
27. Schonenberger, C.; vanderZande, B. M. I.; Fokkink, L. G. J.; Henny, M.; Schmid, C.; Kruger, M.; Bachtold, A.; Huber, R.; Birk, H.; Staufer, U., Template synthesis of nanowires in porous polycarbonate membranes: Electrochemistry and morphology. *Journal of Physical Chemistry B* **1997**, 101, (28), 5497-5505.
28. Whitney, T. M.; Jiang, J. S.; Searson, P. C.; Chien, C. L., Fabrication and magnetic-properties of arrays of metallic nanowires. *Science* **1993**, 261, (5126), 1316-1319.
29. Amblard, J.; Epelboin, I.; Froment, M.; Maurin, G., Inhibition and Nickel Electrocrystallization. *Journal of Applied Electrochemistry* **1979**, 9, (2), 233-242.
30. Cheng, C. L.; Lin, J. S.; Chen, Y. F., Fabrication and growth mechanism of metal (Zn, Sn) nanotube arrays and metal (Cu, Ag) nanotube/nanowire junction arrays. *Materials Letters* **2008**, 62, (10-11), 1666-1669.

31. Grujicic, D.; Pesic, B., Electrodeposition of copper: the nucleation mechanisms. *Electrochimica Acta* **2002**, 47, (18), 2901-2912.
32. Grujicic, D.; Pesic, B., Electrochemical and AFM study of nickel nucleation mechanisms on vitreous carbon from ammonium sulfate solutions. *Electrochimica Acta* **2006**, 51, (13), 2678-2690.
33. Liu, L.; Park, S., Direct Formation of Thin-Walled Palladium Nanotubes in Nanochannels under an Electrical Potential. *Chemistry of Materials* **2011**, 23, (6), 1456-1460.
34. Abd El-Rehim, S. S.; Abd El-Wahab, S. M.; Rashwan, S. M.; Anwar, Z. M., Electroplating of a Co-Cu alloy from a citrate bath containing boric acid. *Journal of Chemical Technology and Biotechnology* **2000**, 75, (3), 237-244.
35. Mohanty, U. S.; Tripathy, B. C.; Das, S. C.; Misra, V. N., Effect of thiourea during nickel electrodeposition from acidic sulfate solutions. *Metallurgical and Materials Transactions B-Process Metallurgy and Materials Processing Science* **2005**, 36, (6), 737-741.
36. Tsuru, Y.; Nomura, M.; Foulkes, F. R., Effects of chloride, bromide and iodide ions on internal stress in films deposited during high speed nickel electroplating from a nickel sulfamate bath. *Journal of Applied Electrochemistry* **2000**, 30, (2), 231-238.
37. Lin, C. S.; Hsu, P. C.; Chang, L.; Chen, C. H., Properties and microstructure of nickel electrodeposited from a sulfamate bath containing ammonium ions. *Journal of Applied Electrochemistry* **2001**, 31, (8), 925-933.
38. Cornelius, T. W.; Apel, P. Y.; Schiedt, B.; Trautmann, C.; Toimil-Molares, M. E.; Karim, S.; Neumann, R., Investigation of nanopore evolution in ion track-etched

polycarbonate membranes. *Nuclear Instruments & Methods in Physics Research Section B-Beam Interactions with Materials and Atoms* **2007**, 265, (2), 553-557.

39. Fleischer, R. L.; Price, P. B.; Symes, E. M., Novel Filter for Biological Materials. *Science* **1964**, 143, (360), 249-250.

40. Ohgai, T.; Hjort, K.; Spohr, R.; Neumann, R., Electrodeposition of cobalt based ferro-magnetic metal nanowires in polycarbonate films with cylindrical nanochannels fabricated by heavy-ion-track etching. *Journal of Applied Electrochemistry* **2008**, 38, (5), 713-719.

41. Keller, F.; Hunter, M. S.; Robinson, D. L., Structural Features of Oxide Coatings on Aluminum. *Journal of the Electrochemical Society* **1953**, 100, (9), 411-419.

42. Masuda, H.; Hasegawa, F.; Ono, S., Self-ordering of cell arrangement of anodic porous alumina formed in sulfuric acid solution. *Journal of the Electrochemical Society* **1997**, 144, (5), L127-L130.

43. Jessensky, O.; Muller, F.; Gosele, U., Self-organized formation of hexagonal pore arrays in anodic alumina. *Applied Physics Letters* **1998**, 72, (10), 1173-1175.

44. Masuda, H.; Yamada, H.; Satoh, M.; Asoh, H.; Nakao, M.; Tamamura, T., Highly ordered nanochannel-array architecture in anodic alumina. *Applied Physics Letters* **1997**, 71, (19), 2770-2772.

45. O Sullivan, J. P.; Wood, G. C., Morphology and Mechanism of Formation of Porous Anodic Films on Aluminum. *Proceedings of the Royal Society of London Series a-Mathematical and Physical Sciences* **1970**, 317, (1531), 511-543.

46. Oniciu, L.; Muresan, L., Some Fundamental Aspects of Leveling and Brightening in Metal Electrodeposition. *Journal of Applied Electrochemistry* **1991**, 21, (7), 565-574.

47. Kollia, C.; Spyrellis, N.; Amblard, J.; Froment, M.; Maurin, G., Nickel plating by pulse electrolysis - Textural and microstructural modifications due to adsorption-desorption phenomena. *Journal of Applied Electrochemistry* **1990**, 20, (6), 1025-1032.
48. Yin, K. M.; Lin, B. T., Effects of boric acid on the electrodeposition of iron, nickel and iron-nickel. *Surface & Coatings Technology* **1996**, 78, (1-3), 205-210.
49. Matlosz, M., Competitive adsorption effects in the electrodeposition of iron-nickel alloys. *J. Electrochem. Soc.* **1993**, 140, (8), 2272-2279.
50. Horkans, J., On the Role of Buffers and Anions in NiFe electrodeposition. *Journal of The Electrochemical Society* **1979**, 126, (11), 1861-1867.
51. Lu, J.; Yang, Q. H.; Zhang, Z., Effects of additives on nickel electrowinning from sulfate system. *Transactions of Nonferrous Metals Society of China* **2010**, 20, S97-S101.
52. Mohanty, U. S.; Tripathy, B. C.; Singh, P.; Das, S. C., Effect of pyridine and its derivatives on the electrodeposition of nickel from aqueous sulfate solutions - Part I: Current efficiency, surface morphology and crystal orientation. *Journal of Applied Electrochemistry* **2001**, 31, (5), 579-583.
53. Mockute, D.; Bernotiene, G., The interaction of additives with the cathode in a mixture of saccharin, 2-butyne-1,4-diol and phthalimide during nickel electrodeposition in a Watts-type electrolyte. *Surface & Coatings Technology* **2000**, 135, (1), 42-47.
54. Chowdhury, T.; Casey, D. P.; Rohan, J. F., Additive influence on Cu nanotube electrodeposition in anodised aluminium oxide templates. *Electrochemistry Communications* **2009**, 11, (6), 1203-1206.
55. Healy, J. P.; Pletcher, D.; Goodenough, M., The chemistry of the additives in an acid copper electroplating bath - the instability of 4,5-dithiaoctane-1,8-disulfonic acid in

- the bath on open circuit. *Journal of Electroanalytical Chemistry* **1992**, 338, (1-2), 167-177.
56. Orinakova, R.; Turonova, A.; Kladekova, D.; Galova, M.; Smith, R. M., Recent developments in the electrodeposition of nickel and some nickel-based alloys. *Journal of Applied Electrochemistry* **2006**, 36, (9), 957-972.
57. Ji, J. X.; Cooper, W. C., Nickel speciation in aqueous chloride solutions. *Electrochimica Acta* **1996**, 41, (9), 1549-1560.
58. Bao, J. C.; Tie, C. Y.; Xu, Z.; Zhou, Q. F.; Shen, D.; Ma, Q., Template synthesis of an array of nickel nanotubules and its magnetic behavior. *Advanced Materials* **2001**, 13, (21), 1631-1633.
59. Cui, C. Q.; Lee, J. Y., Nickel Deposition from Unbuffered Neutral Chloride Solutions in the Presence of Oxygen. *Electrochimica Acta* **1995**, 40, (11), 1653-1662.
60. Hoare, J. P., On the role of boric-acid in the Watts bath. *Journal of the Electrochemical Society* **1986**, 133, (12), 2491-2494.
61. Hoare, J. P., Boric-Acid as a Catalyst in Nickel Plating Solutions. *Journal of the Electrochemical Society* **1987**, 134, (12), 3102-3103.
62. Holm, M.; O'Keefe, T. J., Evaluation of nickel deposition by electrochemical impedance spectroscopy. *Journal of Applied Electrochemistry* **2000**, 30, (10), 1125-1132.
63. Davalos, C. E.; Lopez, J. R.; Ruiz, H.; Mendez, A.; Antano-Lopez, R.; Trejo, G., Study of the Role of Boric Acid During the Electrochemical Deposition of Ni in a Sulfamate Bath. *International Journal of Electrochemical Science* **2013**, 8, (7), 9785-9800.

64. Santos, J. S.; Matos, R.; Trivinho-Strixino, F.; Pereira, E. C., Effect of temperature on Co electrodeposition in the presence of boric acid. *Electrochimica Acta* **2007**, 53, (2), 644-649.
65. Pavlatou, E. A.; Raptakis, M.; Spyrellis, N., Synergistic effect of 2-butyne-1,4-diol and pulse plating on the structure and properties of nickel nanocrystalline deposits. *Surface & Coatings Technology* **2007**, 201, (8), 4571-4577.
66. Nam, D.; Hong, S.; Kim, J.; Lee, J.; Kim, G.; Kwon, H., Synergistic effects of coumarin and cis-2-butene-1,4-diol on high speed electrodeposition of nickel. *Surface and Coatings Technology* **2014**, 248, 30-37.
67. Di Bari, G. A., Electrodeposition of Nickel. In *Modern Electroplating*, 5th ed.; Paunovic, M. S. a. M., Ed. John Wiley & Sons: 2010; p 79.
68. Tsuru, Y.; Nomura, M.; Foulkes, F. R., Effects of boric acid on hydrogen evolution and internal stress in films deposited from a nickel sulfamate bath. *Journal of Applied Electrochemistry* **2002**, 32, (6), 629-634.
69. De Almeida, M. R. H.; Carlos, I. A.; Barbosa, L. L.; Carlos, R. M.; Lima-Neto, B. S.; Pallone, E., Voltammetric and morphological characterization of copper electrodeposition from non-cyanide electrolyte. *Journal of Applied Electrochemistry* **2002**, 32, (7), 763-773.
70. Dudek, D. A.; Fedkiw, P. S., Electrodeposition of copper from cuprous cyanide electrolyte I. Current distribution on a stationary disk. *Journal of Electroanalytical Chemistry* **1999**, 474, (1), 16-30.
71. Dini, J. W.; Snyder, D. D., Electrodeposition of Copper. In *Modern Electroplating*, 4th ed.; Paunovic, M. S. a. M., Ed. John Wiley & Sons: 2000; p 61.

72. Tan, M.; Harb, J. N., Additive behavior during copper electrodeposition in solutions containing Cl⁻, PEG, and SPS. *Journal of the Electrochemical Society* **2003**, 150, (6), C420-C425.
73. Leung, T. Y. B.; Kang, M. C.; Corry, B. F.; Gewirth, A. A., Benzotriazole as an additive for copper electrodeposition - Influence of triazole ring substitution. *Journal of the Electrochemical Society* **2000**, 147, (9), 3326-3337.
74. Bonou, L.; Eyraud, M.; Denoyel, R.; Massiani, Y., Influence of additives on Cu electrodeposition mechanisms in acid solution: direct current study supported by non-electrochemical measurements. *Electrochimica Acta* **2002**, 47, (26), 4139-4148.
75. Mandich, N. V.; Snyder, D. L., Electrodeposition of Chromium. In *Modern Electroplating*, 4th ed.; Paunovic, M. S. a. M., Ed. John Wiley & Sons: 2000.
76. Danilov, F. I.; Vasil'eva, E. A.; Butyrina, T. E.; Protsenko, V. S., Electrodeposition of lead-tin alloy from methanesulphonate bath containing organic surfactants. *Protection of Metals and Physical Chemistry of Surfaces* **2010**, 46, (6), 697-703.
77. Joseph, S.; Phatak, G. J., Effect of additives on the co-electrodeposition of Sn-Ag-Cu lead-free solder composition. *Materials Science and Engineering B-Advanced Functional Solid-State Materials* **2010**, 168, (1-3), 219-223.
78. Tam, T. M., Electrodeposition Kinetics for Tin, Lead, and Tin-Lead Fluorborate Plating Solutions. *Journal of the Electrochemical Society* **1986**, 133, (9), 1792-1796.
79. Jordan, M., Electrodeposition of Tin-Lead Alloys. In *Modern Electroplating*, 5th ed.; Paunovic, M. S. a. M., Ed. John Wiley & Sons: 2010; p 265.

80. Pesco, A. M.; Cheh, H. Y., Current and Composition Distributions during the Deposition of Tin-Lead Alloys on a Rotating Disk Electrode. *Journal of the Electrochemical Society* **1988**, 135, (7), 1722-1726.
81. Kohl, P. A., The High-Speed Electrodeposition of Sn Pb Alloys. *Journal of the Electrochemical Society* **1982**, 129, (6), 1196-1201.
82. Abys, J. A.; Murski, K. J.; Zhang, Y. Electroplating solution for electroplating lead and lead/tin alloys. 2001.
83. Langbein, G., *Electro-deposition of metals a practical, comprehensive work comprising electro-plating, galvanoplastic operations and electrotyping deposition of metals by the contact and immersion processes*. 8th ed.; Henry Carey Baird & Co., Inc: New York, 1920.
84. Erdey-Gruz, T.; Volmer, M., *Z. Phys. Chem. A* **1930**, 150, 201.
85. Frank, F., The influence of dislocations on crystal growth. *Discussions of the Faraday Society* **1949**, 5, 48-54.
86. Burton, W. K.; Cabrera, N.; Frank, F. C., The growth of crystals and the equilibrium structure of their surfaces. *Philosophical Transactions of the Royal Society of London. Series A* **1951**, 299-358.
87. Bewick, A.; Thirsk, H. R.; Fleischmann, M., Kinetics of Electrocrystallization of Thin Films of Calomel. *Transactions of the Faraday Society* **1962**, 58, (479), 2200-2216.
88. Armstrong, R. D.; Harrison, J. A., Two-Dimensional Nucleation in Electrocrystallization. *Journal of the Electrochemical Society* **1969**, 116, (3), 328-331.
89. Scharifker, B.; Hills, G., Theoretical and Experimental Studies of Multiple Nucleation. *Electrochimica Acta* **1983**, 28, (7), 879-889.

90. Sonnenfeld, R.; Schardt, B. C., Tunneling microscopy in an electrochemical-cell - images of Ag-plating. *Applied Physics Letters* **1986**, 49, (18), 1172-1174.
91. Hendricks, S. A.; Kim, Y. T.; Bard, A. J., Imaging of the in situ deposition of lead on highly oriented pyrolytic-graphite by scanning tunneling and atomic force microscopies. *Journal of the Electrochemical Society* **1992**, 139, (10), 2818-2824.
92. Schmidt, W. U.; Alkire, R. C.; Gewirth, A. A., Mechanic study of copper deposition onto gold surfaces by scaling and spectral analysis of in situ atomic force microscopic images. *Journal of the Electrochemical Society* **1996**, 143, (10), 3122-3132.
93. Ikemiya, N.; Yamada, K.; Hara, S., Atomic structures and growth mechanisms of electrodeposited Ag and Te films as discerned by atomic force microscopy. *Journal of Vacuum Science & Technology B* **1996**, 14, (2), 1369-1372.
94. Cao, H.; Wang, L.; Qiu, Y.; Wu, Q.; Wang, G.; Zhang, L.; Liu, X., Generation and growth mechanism of metal (Fe, Co, Ni) nanotube arrays. *Chemphyschem* **2006**, 7, (7), 1500-1504.
95. Liu, L.; Zhou, W.; Xie, S.; Song, L.; Luo, S.; Liu, D.; Shen, J.; Zhang, Z.; Xiang, Y.; Ma, W.; Ren, Y.; Wang, C.; Wang, G., Highly Efficient Direct Electrodeposition of Co-Cu Alloy Nanotubes in an Anodic Alumina Template. *J. Phys. Chem. C* **2008**, 112, (2256-2261).
96. Guo, Y.-Y.; Wand, M.; Mao, X.-B.; Jiang, Y.-X.; Wang, C.; Yang, Y.-L., Growth Mechanism for Controlled Synthesis of Metal Nanotube and Nanowire Arrays Using Anodic Aluminum Oxide Template. *Acta Physico-Chmica Sinica* **2010**, 26, (7), 2037-2043.

97. Zhang, H.-m.; Zhang, X.-l.; Zhang, J.-j.; Li, Z.-y.; Sun, H.-y., Template-Based Electrodeposition Growth Mechanism of Metal Nanotube. *Journal of the Electrochemical Society* **2013**, 160, (2), D41-D45.
98. Tao, F.; Guan, M.; Jiang, Y.; Zhu, J.; Xu, Z.; Xue, Z., An easy way to construct an ordered array of nickel nanotubes: The triblock-copolymer-assisted hard-template method. *Advanced Materials* **2006**, 18, (16), 2161-2164.
99. Pi, Z.; Tian, T.; Yang, C.; Zhang, S.; Zheng, J., A template based electrochemical method for the synthesis of high dense Ni nanotube arrays. *Journal of Nanoscience and Nanotechnology* **2007**, 7, 673–676.
100. Xue, S. H.; Cao, C. B.; Wang, D. Z.; Zhu, H. S., Synthesis and magnetic properties of Fe_{0.32}Ni_{0.68} alloy nanotubes. *Nanotechnology* **2005**, 16, (9), 1495-1499.
101. Lee, W.; Scholz, R.; Niesch, K.; Gosele, U., A template-based electrochemical method for the synthesis of multisegmented metallic nanotubes. *Angewandte Chemie-International Edition* **2005**, 44, (37).
102. Yoo, W.-C.; Lee, J.-K., Field-dependent growth patterns of metals electroplated in nanoporous alumina membranes. *Advanced Materials* **2004**, 16, (13), 1097-1101.
103. Li, D.; Thompson, R. S.; Bergmann, G.; Lu, J. G., Template-based Synthesis and Magnetic Properties of Cobalt Nanotube Arrays. *Advanced Materials* **2008**, 20, (23), 4575-4578.
104. Fukunaka, Y.; Motoyama, M.; Konishi, Y.; Ishii, R., Producing shape-controlled metal nanowires and nanotubes by an electrochemical method. *Electrochemical and Solid State Letters* **2006**, 9, (3), C62-C64.

105. Li, L.; Pan, S. S.; Dou, X. C.; Zhu, Y. G.; Huang, X. H.; Yang, Y. W.; Li, G. H.; Zhang, L. D., Direct electrodeposition of ZnO nanotube arrays in anodic alumina membranes. *Journal of Physical Chemistry C* **2007**, 111, (20), 7288-7291.
106. Xiao, R.; Il Cho, S.; Liu, R.; Lee, S. B., Controlled electrochemical synthesis of conductive polymer nanotube structures. *Journal of the American Chemical Society* **2007**, 129, (14), 4483-4489.
107. Bao, J. C.; Tie, C. Y.; Xu, Z.; Zhou, Q. F.; Shen, D.; Ma, Q., Template synthesis of an array of nickel nanotubules and its magnetic behavior. *Advanced Materials* **2001**, 13, (21).
108. Franklin, T. C., Some mechanisms of action of additives in electrodeposition processes. *Surface & Coatings Technology* **1987**, 30, (4), 415-428.
109. Franklin, T. C.; Chappel, J.; Fierro, R.; Aktan, A. I.; Wickham, R., The role of ion bridging in controlling competitive electrodeposition processes. *Surface & Coatings Technology* **1988**, 34, (4), 515-522.
110. Feng, Z. V.; Li, X.; Gewirth, A. A., Inhibition due to the interaction of polyethylene glycol, chloride, and copper in plating baths: A surface-enhanced Raman study. *Journal of Physical Chemistry B* **2003**, 107, (35), 9415-9423.
111. Healy, J. P.; Pletcher, D.; Goodenough, M., The chemistry of the additives in an acid copper electroplating bath: Polyethylene-glycol and chloride-ion. *Journal of Electroanalytical Chemistry* **1992**, 338, (1-2), 155-165.
112. Yokoi, M.; Konishi, S.; Hayashi, T., Adsorption behavior of polyoxyethyleneglycole on the copper surface in an acid copper-sulfate bath. *Denki Kagaku* **1984**, 52, (4), 218-223.

113. Hope, G.; Brown, G., A study of the adsorption of polymeric additives at a copper electrode and their incorporation into copper deposits by electrodeposition. In *Proceedings of the sixth international symposium on electrode processes*, Wieckowski, A.; Itaya, K., Eds. 1996; Vol. 96, pp 215-226.
114. Gunawardena, G.; Hills, G.; Montenegro, I., Electrochemical nucleation .4. Electrodeposition of copper onto vitreous carbon. *Journal of Electroanalytical Chemistry* **1985**, 184, (2), 357-369.
115. Tourillon, G.; Pontonnier, L.; Levy, J. P.; Langlais, V., Electrochemically synthesized Co and Fe nanowires and nanotubes. *Electrochemical and Solid State Letters* **2000**, 3, (1), 20-23.
116. Davis, D. M.; Podlaha, E. J., CoNiCu and Cu nanotube electrodeposition. *Electrochemical and Solid State Letters* **2005**, 8, (2), D1-D4.
117. Gabe, D. R., The role of hydrogen in metal electrodeposition processes. *Journal of Applied Electrochemistry* **1997**, 27, (8), 908-915.
118. Lischka, M.; Groß, A., Hydrogen on palladium: A model system for the interaction of atoms and molecules with metal surfaces In *Recent Developments in Vacuum Science and Technology*, Dąbrowski, J., Ed. Research Signpost Kerala, India, 2003; pp 111-132.
119. Mitsui, T.; Rose, M. K.; Fomin, E.; Ogletree, D. F.; Salmeron, M., Dissociative hydrogen adsorption on palladium requires aggregates of three or more vacancies. *Nature* **2003**, 422, (6933), 705-707.

120. Supicova, M.; Rozik, R.; Trnkova, L.; Orinakova, R.; Galova, M., Influence of boric acid on the electrochemical deposition of Ni. *Journal of Solid State Electrochemistry* **2005**, 10, (2), 61-68.
121. Zech, N.; Landolt, D., The influence of boric acid and sulfate ions on the hydrogen formation in Ni-Fe plating electrolytes. *Electrochimica Acta* **2000**, 45, (21), 3461-3471.
122. Zeng, H.; Zheng, M.; Skomski, R.; Sellmyer, D. J.; Liu, Y.; Menon, L.; Bandyopadhyay, S., Magnetic properties of self-assembled Co nanowires of varying length and diameter. *Journal of Applied Physics* **2000**, 87, (9), 4718-4720.
123. Frade, T.; Bouzon, V.; Gomes, A.; da Silva Pereira, M. I., Pulsed-reverse current electrodeposition of Zn and Zn-TiO₂ nanocomposite films. *Surface & Coatings Technology* **2010**, 204, (21-22), 3592-3598.
124. Sylla, D.; Rebere, C.; Gadouleau, M.; Savall, C.; Creus, J.; Refait, P. H., Electrodeposition of Zn-Mn alloys in acidic and alkaline baths. Influence of additives on the morphological and structural properties. *Journal of Applied Electrochemistry* **2005**, 35, (11), 1133-1139.
125. Haehnel, V.; Faehler, S.; Schaaf, P.; Miglierini, M.; Mickel, C.; Schultz, L.; Schloerb, H., Towards smooth and pure iron nanowires grown by electrodeposition in self-organized alumina membranes. *Acta Materialia* **2010**, 58, (7), 2330-2337.
126. Wu, J.; Jiang, Y.; Johnson, C.; Liu, X., DC electrodeposition of Mn-Co alloys on stainless steels for SOFC interconnect application. *Journal of Power Sources* **2008**, 177, (2), 376-385.

127. Ji, J.; Cooper, W. C.; Dreisinger, D. B.; Peters, E., Surface pH measurements during nickel electrodeposition. *Journal of Applied Electrochemistry* **1995**, 25, (7), 642-650.
128. Gomez, E.; Muller, C.; Proud, W. G.; Valles, E., Electrodeposition of nickel on vitreous carbon. Influence of potential on deposit morphology. *Journal of Applied Electrochemistry* **1992**, 22, (9), 872-876.
129. Matulis, J.; Slizys, R., On some characteristics of cathodic processes in nickel electrodeposition. *Electrochim. Acta* **1964**, 13, 1177–1188.
130. Harris, T. M., Change in pH near the Cathode During the Electrodeposition of a Bivalent Metal Analysis. *Journal of the Electrochemical society* **1973**, 120, 1034.
131. Durose, A. H., Boric acid in nickel solutions. *Plating and Surface Finishing* **1977**, 64, (8), 52-55.
132. Tilak, B.; Gendront, A.; Mosoiu, M., Borate buffer equilibria in nickel refining electrolytes. *Journal of Applied Electrochemistry* **1977**, 7, 495-500.
133. Gangasingh, D.; Talbot, J. B., Anomalous Electrodeposition of Nickel-iron. *Journal of the Electrochemical Society* **1991**, 138, (12), 3605-3611.
134. Deligianni, H., Effect of Near-Surface pH on Electrodeposition of Iron and Permalloy. *Electrochemical Society Proceedings* **1990**, 90-98, 407-421.
135. Karwas, C.; Hepel, T., Influence of boric-acid on electrodeposition and stripping of Ni-Zn alloys. *Journal of the Electrochemical Society* **1988**, 135, (4), 839-844.
136. Karwas, C.; Hepel, T., Morphology and composition of electrodeposited cobalt-zinc alloys and the influence of boric-acid. *Journal of the Electrochemical Society* **1989**, 136, (6), 1672-1678.

137. Holzle, M. H.; Retter, U.; Kolb, D. M., The kinetics of structural changes in Cu adlayers on Au(111). *Journal of Electroanalytical Chemistry* **1994**, 371, (1-2), 101-109.
138. Palomar-Pardave, M.; Miranda-Hernandez, M.; Gonzalez, I.; Batina, N., Detailed characterization of potentiostatic current transients with 2D-2D and 2D-3D nucleation transitions. *Surface Science* **1998**, 399, (1), 80-95.
139. Philipp, R.; Retter, U., On transition from 2D to 3D nucleation in the anodic film formation of thiourea at the mercury/electrolyte interphase. *Electrochimica Acta* **1995**, 40, (11), 1581-1585.
140. Bosco, E.; Rangarajan, S. K., Some adsorption-nucleation-based models for electrochemical phase formation. *Journal of the Chemical Society-Faraday Transactions I* **1981**, 77, 1673-1696.
141. Lorand, J. P.; Edwards, J. O., Polyol Complexes and Structure of the Benzenboronate Ion. *Journal of Organic Chemistry* **1959**, 24, (6), 769-774.
142. Peters, J. A., Interactions between boric acid derivatives and saccharides in aqueous media: Structures and stabilities of resulting esters. *Coordination Chemistry Reviews* **2014**, 268, 1-22.
143. Whyte, G. F.; Vilar, R.; Woscholski, R., Molecular recognition with boronic acids-applications in chemical biology. *Journal of chemical biology* **2013**, 6, (4), 161-74.
144. Muscatello, M. M. W.; Stunja, L. E.; Asher, S. A., Polymerized Crystalline Colloidal Array Sensing of High Glucose Concentrations. *Analytical Chemistry* **2009**, 81, (12), 4978-4986.

145. Westmark, P. R.; Smith, B. D., Molecular recognition with boronic acids: Boronic acids selectively facilitate glucose-transport through a lipid bilayer. *Journal of the American Chemical Society* **1994**, 116, (20), 9343-9344.
146. Foster, A. B., Iontophoresis Some Disaccharides. *J. Chem. Soc.* **1953**, 1, 982-986.
147. Khym, J. X.; Zill, L. P., The separation of sugars by ion exchange. *Journal of the American Chemical Society* **1952**, 74, (8), 2090-2094.
148. Gauch, H. G.; Dugger, W. M., The role of boron in the translocation of sucrose. *Plant Physiology* **1953**, 28, (3), 457-466.
149. Bull, S. D.; Davidson, M. G.; Van den Elsen, J. M. H.; Fossey, J. S.; Jenkins, A. T. A.; Jiang, Y.-B.; Kubo, Y.; Marken, F.; Sakurai, K.; Zhao, J.; James, T. D., Exploiting the Reversible Covalent Bonding of Boronic Acids: Recognition, Sensing, and Assembly. *Accounts of Chemical Research* **2013**, 46, (2), 312-326.
150. Springsteen, G.; Wang, B. H., A detailed examination of boronic acid-diol complexation. *Tetrahedron* **2002**, 58, (26), 5291-5300.
151. Peak, D.; Luther, G. W.; Sparks, D. L., ATR-FTIR spectroscopic studies of boric acid adsorption on hydrous ferric oxide. *Geochimica Et Cosmochimica Acta* **2003**, 67, (14), 2551-2560.
152. Bouguerra, W.; Mnif, A.; Hamrouni, B.; Dhahbi, M., Boron removal by adsorption onto activated alumina and by reverse osmosis. *Desalination* **2008**, 223, (1-3), 31-37.
153. Demetriou, A.; Pashalidis, I.; Nicolaides, A. V.; Kumke, M. U., Surface mechanism of the boron adsorption on alumina in aqueous solutions. *Desalination and Water Treatment* **2013**, 51, (31-33), 6130-6136.

154. Goldberg, S.; Glaubig, R. A., Boron adsorption on aluminum and iron-oxide minerals. *Soil Science Society of America Journal* **1985**, 49, (6), 1374-1379.
155. Su, C. M.; Suarez, D. L., Coordination of Adsorbed Boron: A FTIR Spectroscopic Study. *Environmental Science & Technology* **1995**, 29, (2), 302-311.
156. Bouguerra, W.; Marzouk, I.; Hamrouni, B., Equilibrium and Kinetic Studies of Adsorption of Boron on Activated Alumina. *Water Environment Research* **2009**, 81, (12), 2455-2459.
157. Su, C. M.; Suarez, D. L., Boron sorption and release by allophane. *Soil Science Society of America Journal* **1997**, 61, (1), 69-77.
158. Sims, J. R.; Bingham, F. T., Retention of boron by layer silicates sesquioxides and soil materials: Iron- and aluminum-coated layer silicates and soil materials. *Soil Science Society of America Proceedings* **1968**, 32, (3), 369-373.
159. Demetriou, A.; Pashalidis, I., Competitive adsorption of boric acid and chromate onto alumina in aqueous solutions. *Water Science and Technology* **2014**, 69, (2), 378-384.
160. Adiga, S. P.; Zapol, P.; Curtiss, L. A., Structure and morphology of hydroxylated amorphous alumina surfaces. *Journal of Physical Chemistry C* **2007**, 111, (20), 7422-7429.
161. Coustet, V.; Jupille, J., High-resolution electron-energy-loss spectroscopy of isolated hydroxyl-groups on alpha-Al₂O₃(0001). *Surface Science* **1994**, 307, 1161-1165.
162. Lefevre, G.; Duc, M.; Lepeut, P.; Caplain, R.; Fedoroff, M., Hydration of gamma-alumina in water and its effects on surface reactivity. *Langmuir* **2002**, 18, (20), 7530-7537.

163. Phan, A.; Cole, D. R.; Striolo, A., Liquid Ethanol Simulated on Crystalline Alpha Alumina. *Journal of Physical Chemistry B* **2013**, 117, (14), 3829-3840.
164. Scheidegger, A. M.; Lamble, G. M.; Sparks, D. L., Spectroscopic evidence for the formation of mixed-cation hydroxide phases upon metal sorption on clays and aluminum oxides. *Journal of Colloid and Interface Science* **1997**, 186, (1), 118-128.
165. Mellis, E. V.; da Cruz, M. C. P.; Casagrande, J. C., Nickel adsorption by soils in relation to pH, organic matter, and iron oxides. *Scientia Agricola* **2004**, 61, (2), 190-195.
166. Strathmann, T. J.; Myneni, S. C. B., Effect of soil fulvic acid on nickel(II) sorption and bonding at the aqueous-boehmite (gamma-AIOOH) interface. *Environmental Science & Technology* **2005**, 39, (11), 4027-4034.
167. Liao, L. X.; Roy, A.; Scheckel, K. G.; Merchan, G.; Selim, H. M., Retention of Nickel in Soils: Sorption-Desorption and Extended X-ray Absorption Fine Structure Experiments. *Soil Science* **2013**, 178, (5), 215-221.
168. Latella, B. A.; Triani, G.; Zhang, Z.; Short, K. T.; Bartlett, J. R.; Ignat, M., Enhanced adhesion of atomic layer deposited titania on polycarbonate substrates. *Thin Solid Films* **2007**, 515, (5), 3138-3145.
169. Frahn, J. L.; Mills, J. A., Paper ionophoresis of carbohydrates: Procedures and results for 4 electrolytes. *Australian Journal of Chemistry* **1959**, 12, (1), 65-89.
170. Sharif, R.; Shamaila, S.; Shaheen, F.; Naseem, S.; Chen, J. Y.; Khaleeq-ur-Rahman, M.; Hussain, K.; Han, X. F., Nanotube wall thickness dependent magnetization reversal properties of NiFe nanotubes. *Journal of Applied Physics* **2013**, 113, (2), 024315.

171. Liu, H. R.; Lu, Q. F.; Han, X. F.; Liu, X. G.; Xu, B. S.; Jia, H. S., The fabrication of CoPt nanowire and nanotube arrays by alternating magnetic field during deposition. *Applied Surface Science* **2012**, 258, (19), 7401-7405.
172. Gillette, E.; Wittenberg, S.; Graham, L.; Lee, K.; Rubloff, G.; Banerjee, P.; Lee, S. B. L., Direct electrodeposition of nanowires in anodized 3D interconnected porous films on aluminium substrates. *Manuscript submitted for publication* **2014**.
173. Kim, D.; Park, D. Y.; Yoo, B. Y.; Sumodjo, P. T. A.; Myung, N. V., Magnetic properties of nanocrystalline iron group thin film alloys electrodeposited from sulfate and chloride baths. *Electrochimica Acta* **2003**, 48, (7), 819-830.
174. Osaka, T.; Asahi, T.; Kawaji, J.; Yokoshima, T., Development of high-performance magnetic thin film for high-density magnetic recording. *Electrochimica Acta* **2005**, 50, (23), 4576-4585.
175. Zhang, Y.; Ivey, D. G., Characterization of Co-Fe and Co-Fe-Ni soft magnetic films electrodeposited from citrate-stabilized sulfate baths. *Materials Science and Engineering B-Solid State Materials for Advanced Technology* **2007**, 140, (1-2), 15-22.
176. Liu, X. M.; Zangari, G.; Shamsuzzoha, M., Structural and magnetic characterization of electrodeposited, high moment FeCoNi films. *Journal of the Electrochemical Society* **2003**, 150, (3), C159-C168.
177. Zhang, Y. H.; Ivey, D. G., Electroplating of nanocrystalline CoFeNi soft magnetic thin films from a stable citrate-based bath. *Chemistry of Materials* **2004**, 16, (7), 1189-1194.
178. Faraday, M., Experimental researches on electricity. *Philosophical Transactions of the Royal Society of London* **1849**, 1.

179. Osaka, T., Recent development of Magnetic recording head core materials by plating method. *Electrochimica Acta* **1999**, 44, (21-22), 3885-3890.
180. Talapatra, S.; Tang, X.; Padi, M.; Kim, T.; Vajtai, R.; Sastry, G. V. S.; Shima, M.; Deevi, S. C.; Ajayan, P. M., Synthesis and characterization of cobalt-nickel alloy nanowires. *Journal of Materials Science* **2009**, 44, (9), 2271-2275.
181. Navas, D.; Asenjo, A.; Jaafar, M.; Pirota, K. R.; Hernandez-Velez, M.; Sanz, R.; Lee, W.; Niesch, K.; Batallan, F.; Vazquez, M., Magnetic behavior of $\text{Ni}_x\text{Fe}_{(100-x)}$ ($65 \leq x \leq 100$) nanowire arrays. *Journal of Magnetism and Magnetic Materials* **2005**, 290, 191-194.
182. Sharif, R.; Shamaila, S.; Shaheen, F.; Naseem, S.; Chen, J. Y.; Khaleeq-ur-Rahman, M.; Hussain, K.; Han, X. F., Nanotube wall thickness dependent magnetization reversal properties of NiFe nanotubes. *Journal of Applied Physics* **2013**, 113, (2), 3.
183. Murphy, M. W.; Kim, P. S. G.; Zhou, X.; Zhou, J.; Coulliard, M.; Botton, G. A.; Sham, T.-K., Biaxial ZnO-ZnS Nanoribbon Heterostructures. *Journal of Physical Chemistry C* **2009**, 113, (12), 4755-4757.
184. Cheng, C.; Fan, H. J., Semiconductor Nanowire Heterostructures: Controlled Growth and Optoelectronic Applications. In *Semiconductor Nanostructures for Optoelectronic Devices NanoScience and Technology* Yi, G.-C., Ed. Springer: New York, 2012; pp 137-166.
185. Svensson, C. P. T.; Seifert, W.; Larsson, M. W.; Wallenberg, L. R.; Stangl, J.; Bauer, G.; Samuelson, L., Epitaxially grown GaP/GaAs $_{1-x}$ P $_x$ /GaP double heterostructure nanowires for optical applications. *Nanotechnology* **2005**, 16, (6), 936-939.

186. Lind, E.; Persson, A. I.; Samuelson, L.; Wernersson, L.-E., Improved subthreshold slope in an InAs nanowire heterostructure field-effect transistor. *Nano Letters* **2006**, 6, (9), 1842-1846.
187. Wang, W.; Lu, X.; Zhang, T.; Zhang, G.; Jiang, W.; Li, X., Bi₂Te₃/Te multiple heterostructure nanowire arrays formed by confined precipitation. *Journal of the American Chemical Society* **2007**, 129, (21), 6702–6703.
188. Dhar, J. C.; Mondal, A.; Singh, N. K.; Chattopadhyay, K. K., Enhanced photoemission from glancing angle deposited SiO_x-TiO₂ axial heterostructure nanowire arrays. *Journal of Applied Physics* **2013**, 113, (17), 174304.
189. Liu, H. L.; She, G. W.; Huang, X.; Qi, X. P.; Mu, L. X.; Meng, X. M.; Shi, W. S., Synthesis and Magnetic Properties of Mn₄Si₇ and Si-Mn₄Si₇ Axial Heterostructure Nanowire Arrays. *Journal of Physical Chemistry C* **2013**, 117, (5), 2377-2381.
190. Huang, Y.-C.; Chen, P.-Y.; Huang, K.-F.; Chuang, T.-C.; Lin, H.-H.; Chin, T.-S.; Liu, R.-S.; Lan, Y.-W.; Chen, C.-D.; Lai, C.-H., Using binary resistors to achieve multilevel resistive switching in multilayer NiO/Pt nanowire arrays. *Npg Asia Materials* **2014**, 6, 1-7.
191. Hu, J. T.; Ouyang, M.; Yang, P. D.; Lieber, C. M., Controlled growth and electrical properties of heterojunctions of carbon nanotubes and silicon nanowires. *Nature* **1999**, 399, (6731), 48-51.
192. Chen, B.; Meng, G.; Xu, Q.; Zhu, X.; Kong, M.; Chu, Z.; Han, F.; Zhang, Z., Crystalline Silicon Nanotubes and Their Connections with Gold Nanowires in Both Linear and Branched Topologies. *Acs Nano* **2010**, 4, (12), 7105-7112.

193. Yang, D.; Meng, G.; Zhang, S.; Hao, Y.; An, X.; Wei, Q.; Ye, M.; Zhang, L., Electrochemical synthesis of metal and semimetal nanotube-nanowire heterojunctions and their electronic transport properties. *Chemical Communications* **2007**, (17), 1733-1735.
194. Rolison, D. R.; Long, J. W.; Lytle, J. C.; Fischer, A. E.; Rhodes, C. P.; McEvoy, T. M.; Bourga, M. E.; Lubers, A. M., Multifunctional 3D nanoarchitectures for energy storage and conversion. *Chemical Society Reviews* **2009**, 38, (1), 226-252.
195. Liu, R.; Duay, J.; Lee, S. B., Heterogeneous nanostructured electrode materials for electrochemical energy storage. *Chemical Communications* **2011**, 47, (5), 1384-1404.